

## Skyrmion Gas Manipulation for Probabilistic Computing

D. Pinna,<sup>1,\*</sup> F. Abreu Araujo,<sup>1</sup> J.-V. Kim,<sup>2</sup> V. Cros,<sup>1</sup> D. Querlioz,<sup>2</sup> P. Bessiere,<sup>3</sup> J. Droulez,<sup>3</sup> and J. Grollier<sup>1</sup>

<sup>1</sup>*Unité Mixte de Physique CNRS, Thales, Université Paris-Sud, Université Paris-Saclay, 91767 Palaiseau, France*

<sup>2</sup>*Centre for Nanoscience and Nanotechnology, CNRS, Université Paris-Sud, Université Paris-Saclay, 91405 Orsay, France*

<sup>3</sup>*Institut des Systèmes Intelligents et de Robotique, Université Pierre et Marie Curie, 75252 Paris, France*



(Received 26 January 2017; revised manuscript received 13 March 2018; published 13 June 2018)

The topologically protected magnetic spin configurations known as Skyrmions offer promising applications due to their stability, mobility, and localization. We emphasize how to leverage the thermally driven dynamics of an ensemble of such particles to perform computing tasks. We propose a device employing a Skyrmion gas to reshuffle a random signal into an uncorrelated copy of itself. This device is demonstrated by modeling the ensemble dynamics in a collective coordinate approach where Skyrmion-Skyrmion and Skyrmion-boundary interactions are accounted for phenomenologically. Our numerical results are used to develop a proof of concept for an energy efficient (approximately in the range of microwatts) device with a low area imprint (roughly on the order of  $\mu\text{m}^2$ ). Whereas its immediate application to stochastic computing circuit designs will be made apparent, we argue that its basic functionality, reminiscent of an integrate-and-fire neuron, qualifies it as an alternative bioinspired building block.

DOI: [10.1103/PhysRevApplied.9.064018](https://doi.org/10.1103/PhysRevApplied.9.064018)

### I. INTRODUCTION

Magnetic Skyrmions promise unique opportunities for the processing, storage, and transfer of information at the intersection of spintronics and nanoelectronics [1–7]. The experimental verification of Skyrmion spin configurations has been a prominent research topic in magnetism over the past decade. Initially observed in bulk noncentrosymmetric crystal lattices [8–12], they have been more recently stabilized in ultrathin ferromagnetic nanostructures strongly affected by the Dzyaloshinskii-Moriya interaction (DMI) resulting from a coupling to a heavy-metal substrate [13,14]. In such materials, Skyrmions are exceptionally stable spin textures capable of enduring room-temperature environments [15–18], and they are manipulable at small current densities ( $10^6$ – $10^{11}$  A/m<sup>2</sup>) [17,19–23]. Furthermore, their topological resilience [2,24] allows them to avoid pinning onto defects [25,26] and guarantees particle number conservation under a wide range of operating conditions [27,28].

The appeal of Skyrmions is so wide that it has defined a field of its own, Skyrmionics, which refers to the emerging technologies based on magnetic Skyrmions as information carriers. In an effort to push for Skyrmion-based electronics, challenges ranging from their creation and annihilation [2,29–31] to the conversion of their topological properties [5,32] to their efficient transmission and readout [2–4,6,33] are being tackled and solved. Recently, proposals have

exploited their nanometric size and high mobility [1,20,26,34] in the context of Skyrmion-based racetrack memories [3,29,35], logic gates [5], voltage-gated transistors [36], and synaptic devices [37]. All such applications typically constrain the Skyrmion motion onto one-dimensional tracks reminiscent of previous device designs seeking to employ domain-wall motion. Very little has been proposed to take advantage of the analogy between Skyrmions and a generic free-moving particle. Specifically, the full two-dimensional freedom of Skyrmion motion has not been leveraged either at a functional level or as a technique to reduce the surface imprint of proposed devices.

All such applications effectively employ geometries where one or more Skyrmions are injected, manipulated, and read out (see Fig. 1). Currently, the standard approach for studying their behavior is to employ micromagnetic simulations capable of modeling the nonlinear evolution of the structure's magnetic texture over time [38]. Whereas micromagnetic techniques can be very precise, the execution time of the finite-difference method they employ scales rapidly with the volume of the structure itself [39]. As such, resolving the behavior of large structures and circuits over long time periods becomes impractical even on the nanosecond scale. It is therefore important to have an efficient method for simulating the behavior of Skyrmion ensembles which scales with the number of Skyrmions instead. Such a technique should be capable of capturing both the influence of magnetic dipole effects, as well as boundary interactions on the ensemble dynamics.

\*dpinna@protonmail.com

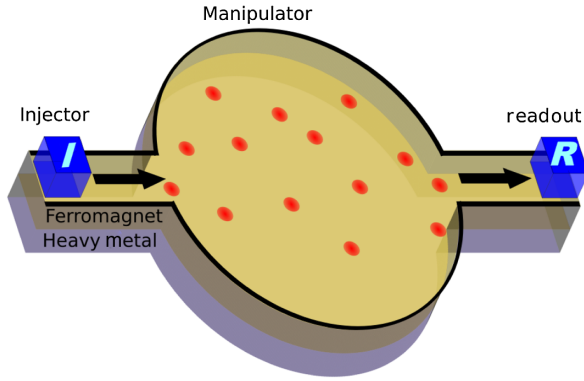


FIG. 1. Bare-bones schematic of a generic Skyrmionic device constructed with a thin-film ferromagnet–heavy-metal bilayer. One or more Skymions are injected into the geometry where manipulation occurs before readout.

At a device level, Skyrmionic applications are not *currently* expected to compete significantly with present-day CMOS implementations of Boolean logic circuits whose strengths lie in the accuracy and precision of bitwise operations. However, limits in the exponential miniaturization of transistor-based architectures expose bottlenecks with regard to both speed and the architectures’ power consumption. This limit is particularly relevant when requiring hardware to enable software capable of performing fast inference over large amounts of data. As an example, much attention has been directed towards the development of artificial neural networks for the execution of deep-learning techniques [40]. Such solutions typically seek to draw inspiration from the probabilistic and massively parallel nature of biological information processing [41], whose virtues have been explored for the past half century [42]. In this context, we propose that greater focus should instead be given to the use of Skymions as basic elements in the design of probabilistic device architectures. By leveraging Skymion number conservation, thermal susceptibility, and ultralow power transport properties, we believe that a fertile route towards disruptive applications can be achieved. Along these lines, our work presents two alternative devices implementing basic building blocks for probabilistic computing.

Starting from the collective coordinate dynamical theory introduced by Thiele [43], this paper develops an  $N$ -body framework capable of modeling the dynamics of Skymion ensembles within their geometries and successively demonstrate how they may be employed to perform probabilistic computing. To this aim, we first, in Sec. II, motivate the deep technological challenges inspiring this work by giving a general background on stochastic computing and justifying the need for a compact and energy-efficient stochastic signal reshuffler, which we propose for employing Skymions as information carriers. In Sec. III, we use micromagnetic simulations to characterize the repulsive Skymion-Skymion and Skymion-boundary interactions.

These interactions then enter phenomenologically into the  $N$ -body Thiele model, where the ensemble dynamics become numerically solvable out to long timescales. These advantages permit us, in Sec. IV, to model the Skymion reshuffler leveraging the full freedom of Skymionic motion. We characterize the device functioning performance and the expected energy consumption. Finally, in Sec. V, we argue how our Skymion reshuffler, subject to minor modifications, can serve a much more general purpose by effectively working as an analog integrate-and-fire neuron [44]. These results lay the groundwork for the application of Skymionic devices as bioinspired building blocks for non-conventional computing strategies.

## II. MOTIVATION: STOCHASTIC COMPUTING

### A. Motivation

As feature sizes in semiconductor systems are scaled down to the point where their deterministic behavior cannot be guaranteed, the necessity for error-correcting codes [45] and hardware redundancies [46,47] has become indispensable for reliable data processing. In this context, *stochastic computing* seeks to embrace probabilistic computing elements to bypass these issues by achieving tremendous gains in signal processing efficiency at the cost of degradation in computational precision [48–52]. Instead of defining operations as precise bitwise manipulations of stored *finite* binary numbers, one instead aims to encode numerical values as the probability of seeing a 1 or 0 in a random sequence of binary bits (*bitstream*, as in Fig. 2 [53]). This probability, known as the  $p$  value, can also be thought of as the statistical ratio of up time to signal length in a random telegraph noise signal. CMOS circuits consisting of cascaded logic gates can then be shown to

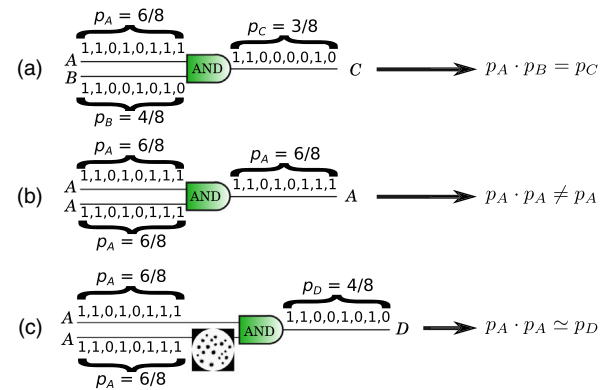


FIG. 2. (a) AND-gate implementation of the multiplication operation under the stochastic computing paradigm. The  $p$  value of the output signal is equal to the product of the input signals’  $p$  values. (b) Whenever correlations exist between the input signals, the AND gate does not perform the expected multiplication. (c) Forcing the input signals through a Skymionic reshuffler allows for a correct multiplication operation even in the presence of strong correlations between the input signals.

perform mathematical operations on the  $p$  values of distinct random streams in real time. We refer to telegraph noise signals and bitstreams interchangeably throughout this paper. Complex circuits have already been proposed to perform operations such as square rooting [54], polynomial arithmetic [55–57], and matrix operations [58], as well as the “tansig” transform function employed in neural networks [59]. The output of such operations results in an output bitstream whose  $p$  value can be read out and, possibly, operated on successively. Last but not least, stochastic computing circuitry is inherently tolerant to faults such as *soft bit flips* [60,61]. Consider the act of randomly flipping one binary bit from a sequence of  $N$  bits (e.g., 010001101  $\rightarrow$  010011101): the binary number encoded changes drastically, while the  $p$  value encoded is altered only by a factor of  $o(1/N)$ .

A very attractive property of stochastic computing is that it enables low-energy cost implementations of arithmetic operations using standard logic elements. As an example, consider the effect of feeding two indefinitely long random streams with  $p$  values of  $p_A$  and  $p_B$  into an AND gate [see Fig. 2(a)]. The AND gate’s properties produce an output signal with a  $p$  value  $p_C = p_A p_B$ , thus implementing the stochastic computing equivalent of multiplication. Whereas the result of the multiplication is produced in real time as the input signals are fed to the AND gate, the accuracy of the result depends on how much of the output signal one wishes to sample. This trade-off of *speed vs accuracy* is central to the development of integrated circuits performing stochastic computing. A detailed description of the initial encoding and tuning or setting of the input  $p$  values goes beyond the scope of this work. We note, however, that, aside from the traditional shift-register-based techniques [62,63], a compact and energy-efficient approach for generating suitable stochastic signals can be achieved through current-biased superparamagnetic magnetic tunnel junctions [64–67], whose individual use in neuromorphic computing architectures has also recently been explored [68–70]. This approach ties in well with the spintronics-based toolbox that can already be used for the nucleation and readout of Skyrmions [14,15], thus allowing for the development of technologically consistent devices [71].

A major issue has, however, impeded the blossoming of stochastic computing as an industrially viable competitor. Namely, cascading gates operating on not fully random signals propagate unwanted correlations rapidly, even after a few elementary operations [52,63,72–75]. In Fig. 2(b), one can immediately see that feeding two identical copies of the same input signal produces an output signal whose  $p$  value does not represent a product operation in any way. It is, therefore, crucial to be able to regularly reshuffle signals so that they stay uncorrelated. We call this element a stochastic reshuffler, capable of *copying* an input stream into an uncorrelated new one while preserving the original  $p$  value. By prefixing such devices to each gate in a circuit

[see Fig. 2(c)], inconvenient correlations can be washed out effectively.

At this time, no efficient hardware stochastic reshufflers are known to exist. In CMOS, reshuffling signals can be done by combining a pseudorandom number generator with a shift register or counter (both requiring long-term memories) [76]. This means that each reshuffling operation has a large area imprint (a typical integrated shift register has a linear size of about 10–100  $\mu\text{m}$ ) and consumes a lot of energy. It is, therefore, impossible to insert these reshufflers after each calculation stage in a stochastic computing circuit, preventing the realization of any large-scale demonstration of stochastic computing on chip. To overcome these technological obstacles, we propose an alternative reshuffler design as the first low-energy, compact device proposal of its kind: the Skyrmion reshuffler [77].

## B. Skyrmion reshuffler

Our original concept converts an input bitstream into a sequence of Skyrmions whose order can be thermally reshuffled due to the diffusive two-dimensional dynamical nature of interacting Skyrmions at finite temperature. If the order of this sequence can be altered enough by the thermal noise affecting Skyrmion motion inside the device geometry, the new Skyrmion sequence can then be *read* as a new uncorrelated output signal with a  $p$  value identical to that of the input signal.

The device (depicted in Fig. 3) consists of two circular chambers with input-output conduit tracks capable of ushering Skyrmions into and out of the chambers. The net drift of Skyrmions is achieved by a static current

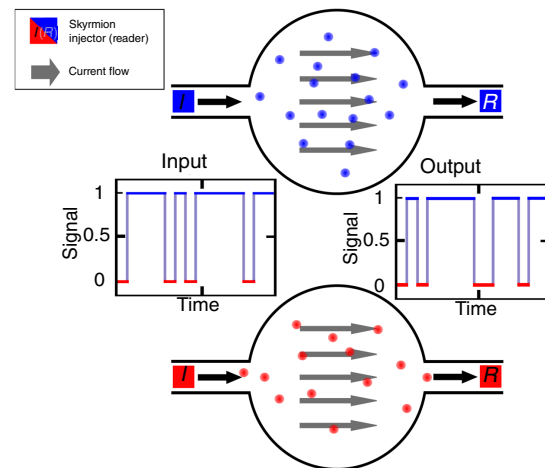


FIG. 3. The proposed device consists of two magnetic chambers into which Skyrmions are injected depending on the state of an input telegraph noise signal. The net drift of the Skyrmion particles due to a constant current flow along with the thermal diffusion in the chambers leads to an exit order that can be significantly different from that of entry. This behavior is employed to reconstruct a new outgoing signal with the same statistical properties as the first, as well as being uncorrelated from it.

flowing across the entire structure from one conduit to the other (see Sec. VI). Skyrmions injected can be nucleated singularly via the injection of localized spin currents with magnetic tunnel junctions (MTJs) [3], using in-plane spin torques on a notch [25], by rapid proliferation with appropriately constructed input conduit geometries [15,78], or via a periodic shedding off of material defects with homogeneous dc currents [79]. Analogously, the readout elements can consist of MTJs capable of measuring magnetoresistance changes due to the passing of Skyrmions through the underlying magnetic layer [80]. We summarily assume injection or detection capabilities by providing each track with an injection or detection element.

The up-and-down (binary) states of the bitstream are used to select which chamber to inject the generated Skyrmions into (see Fig. 3). We do so by selectively nucleating Skyrmions at a constant rate ( $r_{\text{inj}} = 0.2$  nucleations/ns in the simulations presented here) onto the input conduit of one of the two chambers (up and down) depending on the input signal's state. Doing so generates a total population of  $N$  Skyrmions proportional to the length  $\tau_{\text{input}}$  of the input signal ( $N = r_{\text{inj}}\tau_{\text{length}}$ ) and chamber populations  $N_{\text{up}} = pN$  and  $N_{\text{down}} = (1-p)N$  given by the  $p$  value of the input signal. The current-induced drift then pushes the Skyrmions across their respective chambers towards the output track where they are detected. The sequence of outgoing Skyrmions can then be decodified into an outgoing signal. Whenever an outgoing Skyrmion is read out from the up (down) chamber we switch the outgoing signal into an *up* (*down*) state. As a result of this procedure, the output signal's length is given by the time  $\tau_{\text{output}}$  taken to read all of the Skyrmions and, by construction, its  $p$  value is identical to that of the input signal as long as the relative Skyrmion particle numbers in the chambers are conserved. The basic operating principles of the Skyrmion reshuffler allow it to also work as a device capable of generating stochastic bitstreams with well-defined  $p$  values. To do so, it suffices to inject Skyrmions into the two chambers with a specified ratio and allowing the reshuffling to scramble the input order into a random outgoing Skyrmion sequence.

In order to quantify the performance of Skyrmion reshuffling as a function of chamber materials and geometries, we first model the dynamics of thermally diffusing assemblies of interacting Skyrmions.

### III. MODELING THE DYNAMICS OF INTERACTING SKYRMIONS

#### A. Isolated Skyrmion dynamics

The motion of an isolated Skyrmion in a two-dimensional film can be described by a modified version of Newton's equation which tracks the coordinate evolution of the Skyrmion's center. Assuming translational invariance

of the Skyrmionic spin texture, the *Thiele* equation of motion can be used [4,43,81,82]:

$$\hat{\mathbf{G}}^\alpha \cdot \dot{\mathbf{x}} = \mu \hat{\mathbf{G}}^\eta \cdot \mathbf{v}_s + \mathbf{F}_{\text{Th}} + \mathbf{F}_{\text{ext}}, \quad (1)$$

$$\hat{G}_{ij}^\sigma = G\epsilon_{ij} + \sigma D\delta_{ij}, \quad (2)$$

where  $\hat{\mathbf{G}}$  is the gyrotropic matrix,  $\epsilon_{ij}$  is the Levi-Civita tensor,  $\delta_{ij}$  is a Krönecker  $\delta$ , and the  $\sigma$  in Eq. (2) is equal to either the damping constant  $\alpha$  [when referring to the left side of Eq. (1)] or a parameter  $\eta$  characterizing both the net ratio of adiabatic and nonadiabatic spin-torque intensities and the ratio of dampinglike to fieldlike torques depending on the geometries of current injection. Doing so, our model is general enough to capture equally well the Skyrmion driving motion originating from both spin torques due to in-plane currents as well as spin-orbit torques arising from the underlying heavy-metal layer [26,83,84]. Last, the parameter  $\mu$  models the net intensity due to the combination of these two driving effects. Time is in units of  $\gamma M_s$ , where  $\gamma$  is the gyromagnetic ratio and  $M$  the magnetic texture's local moment magnitude. Under the assumption of an invariant Skyrmion profile, the gyrotropic matrix (2) is composed of the gyrovector  $G$ , a topological invariant arising from the *twist* in the spin texture, and the dissipative damping diadic  $D$ , which, together with  $\alpha$ , characterizes the net friction acting on the Skyrmion [43,82,83,85,86]. Both are typically computed explicitly from the static magnetic profile:

$$G = \int d\mathbf{r} \mathbf{n} \cdot (\partial_x \mathbf{n} \times \partial_y \mathbf{n}), \quad (3)$$

$$D = \int d\mathbf{r} (\partial_x \mathbf{n} \cdot \partial_x \mathbf{n} + \partial_y \mathbf{n} \cdot \partial_y \mathbf{n})/2, \quad (4)$$

where  $\mathbf{n}$  is the local, unit-normalized magnetization orientation. A very convenient property of both terms is that they do not scale with the Skyrmion's size as long the Skyrmion is larger than a few times the domain-wall width  $\sqrt{A_{\text{ex}}/K_u}$  (where  $A_{\text{ex}}$  and  $K_u$  are the material exchange constant and the perpendicular magnetic anisotropy, respectively). This property ensures that their values computed in zero-temperature micromagnetic simulations are also valid for the modeling of finite-temperature Skyrmions. Thermal effects are known, in fact, to excite extra degrees of freedom capable of altering the Skyrmion profile, such as breathing modes [87] and oscillations in the domain-wall angle [88]. These effects are expected to qualitatively alter the dynamics of large Skyrmions (of about 200 nm), where second-order inertial terms should be included in the respective Thiele models [86,89]. For the physical parameters chosen in our simulations (see Sec. VI), we find stable isolated Skyrmions with a typical diameter of approximately 39 nm and no effective inertial mass. Whereas the thermal-noise effects in the micromagnetic simulations lead to fluctuations of the Skyrmion radius, they are found to take place on short timescales at a nanosecond

level (compared to the length of the simulated dynamics) and do not affect our treatment.

The three force terms appearing on the right side of Eq. (1) model various interactions that dynamical Skyrmions are subject to. Both the conduction of electrons through the spin texture and the pumping of spin through spin-orbit-torque effects are known to induce both an adiabatic and a non-adiabatic spin torque [90] (usually referred to as dampinglike or fieldlike spin torques when spin-orbit torques are considered), giving rise to well-defined force components acting on the Skyrmion profile [81,91]. These current-induced drift effects are captured by the first term where  $\mathbf{v}_s$  is the spin-drift velocity (directly proportional to the current density  $j$ ). In the special case where  $\eta = \alpha$ , Skyrmions drift along the current flow lines. In all other circumstances, however, the discrepancy between  $\alpha$  and  $\eta$  leads to current-induced Skyrmion flows which proceed at an angle to the current flow driving them [3,21].

Similarly, the thermal forces are modeled by the collective action of independent random magnetic fields acting on the texture's local magnetic moments. The net effect results in an additive, homogeneous zero-mean stochastic term in the Thiele dynamics [92,93]:

$$\langle \mathbf{F}_{\text{Th}} \rangle = 0, \quad (5)$$

$$\langle F_{\text{Th},i}(t) F_{\text{Th},j}(t') \rangle = 2\alpha D \frac{k_B T}{\gamma M} \delta_{i,j} \delta(t-t'), \quad (6)$$

where  $k_B T$  is the thermal energy and  $\langle \dots \rangle$  represents the averaging over noise realizations. From Eq. (1), the mean-squared displacement of Skyrmions can be expected to scale linearly in time with the diffusion constant given by

$$\langle |\mathbf{x}|^2 \rangle(t) = 2k_B T \frac{\alpha D}{G^2 + (\alpha D)^2} t. \quad (7)$$

The remaining term, which we now proceed to discuss in detail, seeks to model all repulsive inter-Skyrmion interactions and boundary effects:

$$\mathbf{F}_{\text{ext}} = \mathbf{F}_S + \mathbf{F}_B, \quad (8)$$

where  $\mathbf{F}_S$  and  $\mathbf{F}_B$  are, respectively, Skyrmion-Skyrmion and boundary repulsion terms.

As described in Appendix A, we mainly consider magnetic materials with a saturation magnetization  $M_S = 1400$  kA/m, an exchange stiffness  $A_{\text{ex}} = 27.5$  pJ/m, an interface-induced DMI constant  $D = 2.05$  mJ/m<sup>2</sup>, a perpendicular magnetic anisotropy constant  $K_u = 1.45$  MJ/m<sup>3</sup>, and  $\alpha = 0.1$ . The choice of these values is consistent with interfacially stabilized Skyrmions on Pt/Co/MgO nanostructures [18].

## B. Skyrmion interactions

Short-range repulsions between Skyrmions due to exchange-dominated deformations to their respective spin

textures have already been theoretically and numerically discussed in the literature in the absence of magnetic dipole effects [26]. However, dense Skyrmion populations are known to exhibit long-range order leading to the formation of regular lattice structures [13,17,34], for which dipole interactions may play a relevant role. To capture the net sum of these effects on a single Skyrmion's Thiele dynamics, we introduce a force term  $F_S$  in Eq. (8) which sums all the two-body interactions among Skyrmions in a given ensemble (in the vein of Eq. [26]):

$$\mathbf{F}_S = \sum_j \mathbf{F}_{S-S}(\mathbf{d}_{ij}), \quad (9)$$

$$\mathbf{F}_{S-S}(\mathbf{d}) = \exp\left[-\frac{a_1 d^2 + a_2 d + a_3}{d+1}\right] \hat{\mathbf{d}}, \quad (10)$$

where  $d_{ij}$  is the distance between particles  $i$  and  $j$ , and  $\hat{\mathbf{d}}$  is the normalized distance vector. The specific exponential form is chosen such that the repulsion behaves Gaussian-like at short range and scales like a simple exponential at distances greater than the typical Skyrmion diameter.

Whereas the long-range exponential scaling is justified in the thin-film limit where stray field energies can be modeled by a local shape anisotropy (see Appendix B), the short-range Gaussian scaling is chosen to fit the micromagnetic behavior observed at small inter-Skyrmion distances. In fact, for separation distances smaller than the Skyrmion diameter, the notion of a Skyrmion as a particle is expected to lose its meaning since the complexity of the magnetic texture voids the assumptions giving rise to the Thiele approximation. As such, even though we include a Gaussian correction to the Skyrmion repulsion, we do not consider scenarios where this correction is relevant. This limit typically happens whenever the interparticle spacing is smaller than the average Skyrmion diameter.

To fit the phenomenological parameters  $a_k$  (see Sec. VI for values), we perform micromagnetic simulations far from boundaries where the net two-body skyrmion-skyrmion interaction in the presence of dipole effects can be isolated. Two Skyrmions are initially set at a very close distance from each other and allowed to relax over time (see Sec. VI for details).

In Fig. 4, we plot the gyrotropic matrix elements obtained by using Eqs. (3) and (4) from the evolving magnetic profiles. Both  $G$  and  $D$  are seen to quickly stabilize onto equilibrium values, with  $G = -4\pi$ , as expected from the Skyrmion's topological charge and core orientation in the continuum limit [94]. Employing these values, the net repulsion force between the two particles is extracted by computing  $\hat{\mathbf{G}} \cdot \dot{\mathbf{x}}$  [the left-hand side of Eq. (1)] as the simulation progresses. This result, in turn, allows for the exploration of how the net repulsion force scales with the inter-Skyrmion distance. Figure 5 shows the particle trajectories (left panel) along with the extracted repulsion

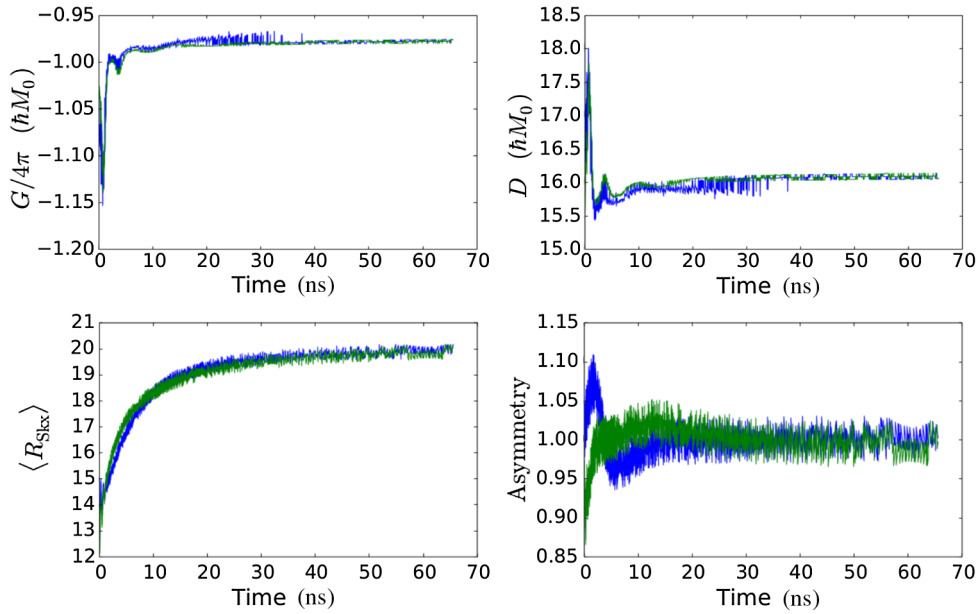


FIG. 4. Two Skyrmions, initially separated by 50 nm, are allowed to evolve, via micromagnetic simulation, for 65 ns in the absence of thermal noise and applied currents. The topological constants are shown as a function of time. After a very brief relaxation phase, both the gyrovector  $G$  (left panels) and the dissipative dyadic  $D$  (right panels) stabilize around fixed values. Numerical deviations from constancy are due to the limited magnetic texture that is considered when performing integrals (3) and (4). To better qualify the relaxation process, the average Skyrion radius and Skyrion asymmetry (a value of 1.0 representing perfectly circular particles) are plotted as a function of time.

force as a function of interparticle distance in units of Skyrion diameter (right panel). We find that the fit (10) is adequate in modeling the observed two-body repulsion resulting from exchange and dipolar interactions. Specifically, we note that the Gaussian corrections to Eq. (10) are only relevant at interparticle distances smaller than the average Skyrion diameter.

### C. Boundary effects

Skyrmions are experimentally studied on finite geometries. As such, it is essential to account for how the particle dynamics may be affected by the geometry's boundaries. The radial size of isolated Skyrmions in magnetic dots is known to be confined by an explicit condition on the

orientation of magnetic moments at the boundary [3,95]. This effect, a direct result of the DMI in the material, is also responsible for repelling Skyrmions from boundaries, thus guaranteeing the transport properties which make them so useful for applications [3,21]. As Skyrmions in rarefied ensembles (as opposed to lattices) are capable of moving about freely, their dynamics eventually lead them close enough to the sample boundary where their behavior must be quantified through the Thiele formalism.

We repeat our previous phenomenological analysis to model boundary effects by extracting the net force experienced by a solitary Skyrion initially placed adjacent to the boundary of a circular geometry. In Fig. 6, the force experienced by the Skyrion results in a net drift both along and away from the dot's boundary (left panel), whose

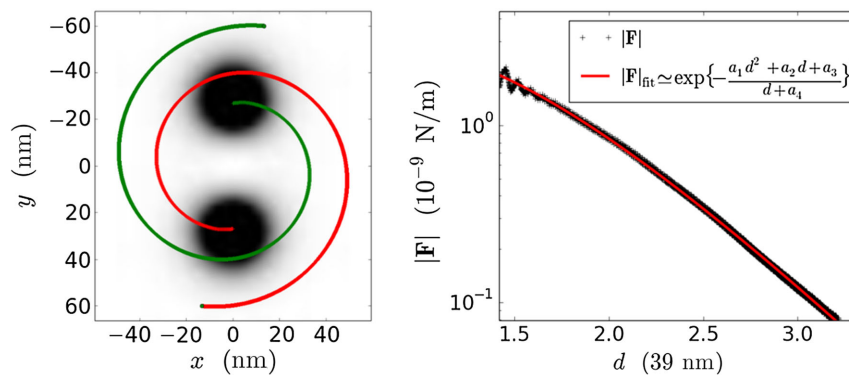


FIG. 5. Two Skyrmions, initially separated by 50 nm, are allowed to evolve for 65 ns in the absence of thermal noise and applied currents. Their extracted trajectories (left panel) are employed to compute the inter-Skyrmion repulsion-force intensity (right panel), plotted as a function of distance in units of an average Skyrion diameter (approximately 39 nm), which is then fit phenomenologically according to Eq. (10). Over the course of the simulation, the two Skyrmions are seen to spiral away from each other as a direct consequence of the gyrotropic terms appearing in the Thiele-dynamical model (an initial frame of the simulation showing the Skyrion initial position is given for reference).

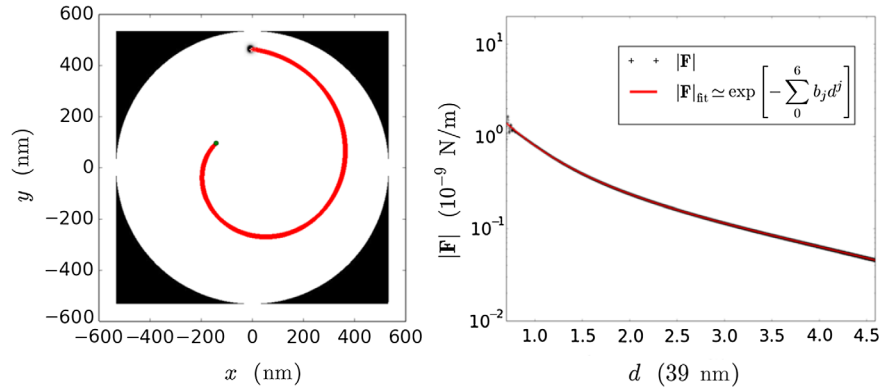


FIG. 6. Net force experienced by a solitary Skyrmion initially nucleated at a distance of  $d = 50$  nm from the boundary of a 1024-nm-diameter circular geometry and allowed to evolve for  $1 \mu\text{s}$ . Over the course of the simulation, the Skyrmion's trajectory (left panel) is seen to move—clockwise—both along and away from the magnetic boundary (the thick black curve) as a result of the gyrotropic effects captured by the Thiele-dynamical model (an initial frame of the simulation showing the Skyrmion initial position is given as reference). The red line (right panel) shows a fit to the numerically derived force as a function of the distance from the boundary in units of the average Skyrmion diameter.

scaling behavior as a function of distance from the boundary is distinctly different from that observed for Skyrmion-Skyrmion repulsions. In order to have an explicit phenomenological expression for the boundary repulsion force, we fit the observed data to a sextic Gaussian form (see Sec. VI):

$$|\mathbf{F}|_B \simeq \exp\left[-\sum_0^6 b_j d^j\right], \quad (11)$$

which is found to model the boundary interaction very well.

Neither the Skyrmion-Skyrmion nor the Skyrmion-boundary interaction should be considered valid when distances become smaller than the Skyrmion diameter. At such length scales, the topological texture of each

Skyrmion is radically altered, leading to a behavior that is not consistent with either the Thiele dynamical model or the notion of topologically protected particles. When Skyrmions are moved too close to each other or to boundaries, annihilation typically ensues what, if anything, should be modeled via an attractive (rather than repulsive) force law [96].

#### D. Ensemble dynamics

Having modeled both two-particle and boundary repulsions, we now proceed to verify the assumptions of our model. We repeat the same numerical procedures for larger Skyrmion numbers to verify that effective forces perceived by single Skyrmions can be reconducted to an  $n$ -body sum

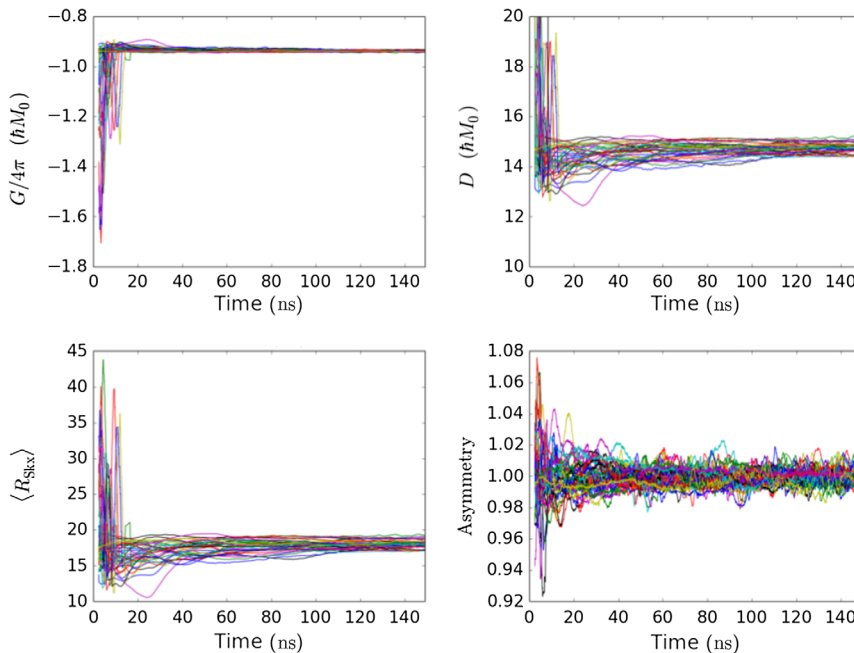


FIG. 7. 47 Skyrmions, initially placed randomly inside a 1024-nm-diameter circular geometry, are allowed to evolve for 150 ns in the absence of thermal noise and applied currents. The topological constants are shown as a function of time. After a very brief relaxation phase, both the gyrovector  $G$  (left panels) and the dissipative dyadic  $D$  (right panels) stabilize around fixed values. The numerical deviations from constancy are due to the limited magnetic texture that is considered when performing integrals (3) and (4).

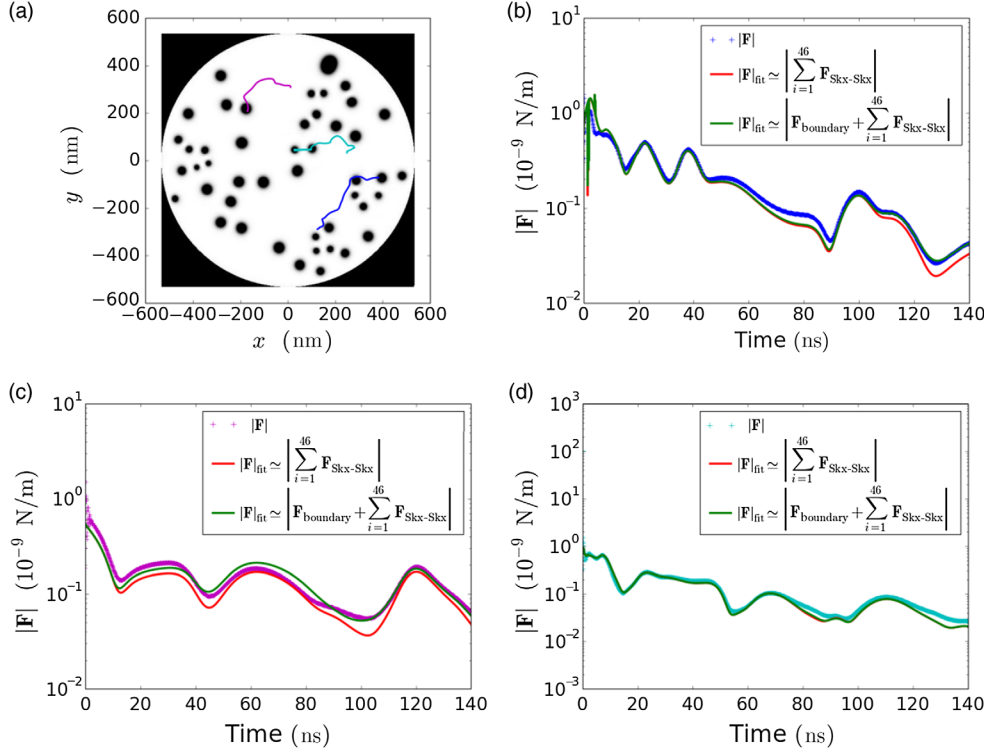


FIG. 8. 47 Skyrmions, initially placed randomly inside a 1024-nm-diameter circular geometry, are allowed to evolve for 150 ns in the absence of thermal noise and applied currents. (a) Their extracted trajectories are then used (an initial frame of the simulation showing the Skyrmion initial positions is given as reference), in conjunction with their extracted gyrotropic constants [see Fig. 7 and Eq. (1)], (b)–(d) to compute the effective forces acting on each particle ( $\mathbf{F}_{\text{ext}} = \hat{\mathbf{G}}^\alpha \cdot \dot{\mathbf{x}}$ ). The net forces acting on each sampled Skyrmion is shown (the colored crosses) and compared to the additive two-Skyrmion prediction (9)—both with and without the boundary interaction term (the green and red fits, respectively)—to exemplify the importance of all of the effects discussed in the text.

of individual two-particle repulsions plus a boundary interaction term. We simulate 47 Skyrmions initially placed randomly inside a circular geometry and allowed them to evolve for 150 ns. In Fig. 7, we again see how the gyrotropic matrix elements of each Skyrmion are consistent (within a 10% margin of error) with those found for the two-particle simulation in Fig. 4. In our particle treatment of the ensemble dynamics, we use identical Thiele parameters for every Skyrmion, as justified by the small error of our micromagnetically derived gyrotropic constants.

As discussed for the two- and one-particle studies of the previous sections, we reconstruct the net force experienced by each Skyrmion from its trajectory and the gyrotropic parameters obtained from the two-Skyrmion simulation. In Fig. 8, the dynamics of three sample Skyrmions are tracked and their net force extracted from the simulated dynamics. We compare this force to our phenomenological expressions accounting for just the Skyrmion-Skyrmion interactions (9) (the red curves) and the case where boundary interactions are also included (11) (the green curves). The additional boundary term  $\mathbf{F}_B$  is included to highlight its importance in modeling Skyrmions in the vicinity of the boundary, resulting in a much better fit. Particularly, the boundary effects only become important when Skyrmions approach the boundary. As an example, in Fig. 8(d), a particle whose trajectory stays close to the center of the nanodot is shown. In this circumstance, the particle’s force fit with and without the boundary correction term are found to be virtually identical. The excellent agreement between micromagnetic simulations and our fit demonstrates that

our multibody Thiele model sufficiently captures dipolar and exchange Skyrmion-Skyrmion interactions as well as Skyrmion-boundary interactions. With these tools in hand, we now proceed to efficiently model the dynamics of large ensembles of Skyrmions in a device setting.

#### IV. SKYRMION RESHUFFLER

Having evaluated the behavior of single Skyrmions in a confined system and extracted the forces and topological parameters of interacting Skyrmions, as well as the influence of sample boundaries, the next step towards the implementation of bioinspired Skyrmion-based devices is to apply the numerical techniques developed to simulate an actual real-world device. We begin with the Skyrmion reshuffler introduced in Sec. II, then propose a completely different application of the same device as a neuron in Sec. III. Many other future devices employing the same principles as ours should be possible and should be numerically tractable via the modeling techniques just introduced.

We simulate the Skyrmion reshuffler in Fig. 3 by considering two identical circular 1024-nm chambers into which we inject Skyrmions every 5 ns, depending on the state of a 0.5-ms-long telegraph noise signal with a fixed  $p$  value. The Skyrmions are initially injected from 100-nm-wide input conduits with currents of varying intensity (see Sec. VI). After drifting and diffusing through their respective chambers, they are then read upon arriving at the output track and used to reconstruct an outgoing signal. The output

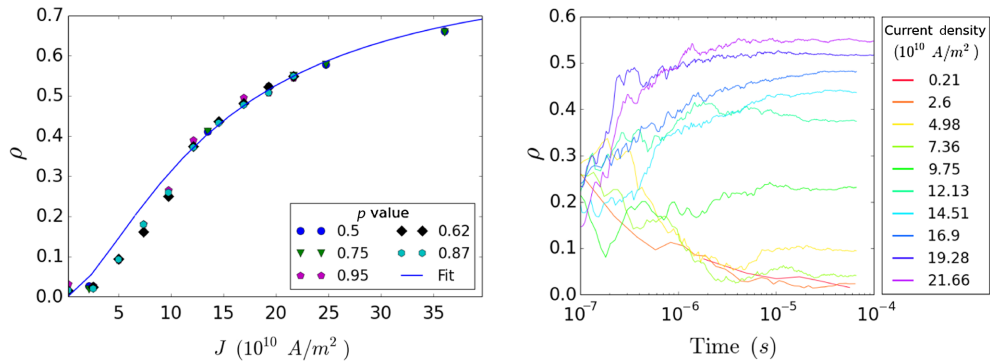


FIG. 9. Simulation of the Skyrmion reshuffler operating at a temperature of 300 K employing two identical chambers (with 1024-nm diameters) to scramble 0.5-ms-long, randomly generated telegraph noise input streams for different current intensities as measured at the 100-nm-wide conduits. (Right panel) Temporal evolution of correlation as the output stream is generated (data correspond to the  $p = 0.62$  simulation). (Left panel) Final product-moment correlation coefficient at each current intensity for five different input  $p$  values. The blue curve fits data to the scaling  $\rho = c_A/(c_B + J^{-3/2})$  argued for in the discussion following Eq. (14).

signal's correlation to the input is then checked by computing the product-moment correlation coefficient of the two [97]:

$$\rho_{X,Y} = \frac{\mathcal{C}(X,Y)}{\sigma_X \sigma_Y}, \quad (12)$$

where  $\mathcal{C}(X,Y)$  is the covariance of two signals  $X$  and  $Y$ , while  $\sigma$  is their respective variance. We show this result in Fig. 9 as a function of the drift current intensity for different signal  $p$  values.

If the chamber is significantly larger than the transverse size of the input-output conduit tracks, current densities inside the chamber may become small enough, allowing Skyrmions to interact and diffuse thermally in the chambers before exiting. In Fig. 9 (left panel), the correlation coefficient  $\rho$  is, in fact, seen to decrease rapidly with lower current intensities. For the physical values considered, our device shows that strong decorrelation is achieved for currents intensities of about  $10^{10}$  A/m<sup>2</sup>. For the lowest currents sampled, no more than 51 particles are observed in either chamber at any given time. As we see later on (see Fig. 13), this number is well below the saturation limit of 90 for this chamber size. From the moment the output signal reconstruction commences, the correlation reaches its steady-state value on a microsecond timescale, as can be seen in Fig. 9 (right panel) with the flattening of the correlations' temporal traces. The time required to inject and read out a statistically significant number of Skyrmions determines the precise timescale for relaxation of correlations towards their steady-state equilibrium. This notion leads to the intuitive understanding that stronger currents allow the device to function faster, at the cost of decorrelation efficiency. In turn, what exactly qualifies as ‘‘satisfactory decorrelation’’ ultimately depends on the details and specifications of the stochastic computing circuit one wishes to implement. Furthermore, we do not see

significant deviations in the results as a function of the  $p$  value assigned to the input signal. In Fig. 10, we instead fix the current intensity at  $1.7 \times 10^{11}$  A/m<sup>2</sup> and allow the chamber sizes to vary. Larger chambers allow the particles to diffuse for longer, thus resulting in a better decorrelation of the shuffler's output signal. Ultimately, Figs. 9 and 10 show how the degree of decorrelation achieved can be tuned by lowering the current intensity and/or increasing the chamber sizes.

Ideally, one would like the signal scrambler to work as fast as possible. The speed at which a statistically significant output signal can be generated depends directly on the intensity of the driving current moving the injected Skyrmions through the chambers (we neglect effects due to finite response times of nucleation and readout mechanisms).

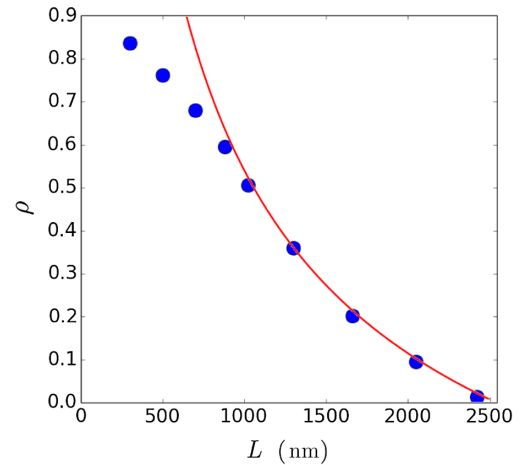


FIG. 10. Output signal correlation as a function of different chamber sizes driven at a current intensity of  $1.7 \times 10^{11}$  A/m<sup>2</sup>. Increasing the chamber size results in a longer diffusion time of the particles inside the chamber, leading to a better decorrelation of the output signal. The red curve fits data to the scaling  $\rho = c_A + c_B/\sqrt{L}$  argued for in the discussion following Eq. (14).

However, as shown in Fig. 9, higher currents lead to highly correlated output signals due to the fact that Skyrmion particles do not spend enough time diffusing and interacting in the chambers. In Fig. 9 (left panel), we find a 64% correlation at the highest driving current sampled ( $3.8 \times 10^{11}$  A/m<sup>2</sup>).

Alternatively, one may try to increase the temperature in an attempt to amplify thermal diffusion. This increase in temperature, however, leads to both a higher energetic consumption and the potential for an increased Skyrmion annihilation rate. Alternatively, one could attempt to leverage the presence of random material inhomogeneities to further drive the diffusive processes. This approach has recently been discussed and characterized in the literature [98] as a possible technique to tune the Skyrmion dynamical properties. Ultimately, the condition affecting this trade-off lies in the relative intensity of dynamical drift and thermal noise. From Eq. (7), one has that the Skyrmion's diffusivity over time results in a dispersion given by

$$\langle |\mathbf{x}|^2 \rangle(t) = 2 \frac{k_B T}{\gamma M} \left( \frac{\alpha D}{G^2 + (\alpha D)^2} \right) t, \quad (13)$$

where  $t$  is the elapsed time and angle brackets  $\langle \dots \rangle$  refer to averaging over noise.

Significant decorrelation between input and output signals takes place whenever this diffusion is large enough to allow scrambling in the sequence of Skyrmions being injected into the chamber. Denote then by  $l_0$  the relative spacing between successively injected Skyrmions. If thermal effects manage to displace Skyrmions more than their interspacing ( $\langle |\mathbf{x}| \rangle \gg l_0$ ) over the time it takes them to cross the chamber, it is reasonable to expect the ingoing and outgoing sequences to become randomized relative to each other. As such, a qualitative estimate of the correlation between the input and outgoing signals can be found in the ratio between these two length scales  $\rho \propto 1/(1 + \sqrt{\langle |\mathbf{x}|^2 \rangle}/l_0)$ . Recalling then from Eq. (1) that the particle drift speed scales with the current intensity ( $|\dot{\mathbf{x}}| \simeq \mathbf{v}_s \propto J$ ), one can expect that correlations will scale relative to system parameters as

$$\frac{\rho}{1-\rho} \propto \frac{l_0}{\sqrt{\langle |\mathbf{x}|^2 \rangle}(t_{\text{exit}})} \propto \nu \sqrt{\frac{\gamma M}{k_B} \left( \frac{G^2 + \alpha D^2}{\alpha D} \right) \frac{J^3}{LT}}, \quad (14)$$

where we denote the chamber diameter as  $L$  and the injection frequency as  $\nu$ , the time taken to cross the chamber is  $t_{\text{exit}} \simeq L/|\mathbf{v}_s| \propto L/J$  and the interparticle spacing is  $l_0 \propto \nu J$ . The fitting curves in Figs. 9 and 10 indeed verify that the scalings  $\rho/(1-\rho) \propto J^{3/2}/\sqrt{L}$  match our numerical data, thus justifying how correlations will be lower for smaller currents and larger chamber sizes.

A potential improvement to the Skyrmion reshuffler can theoretically be found in the use of antiferromagnetic (AFM) materials, where the possibility of stabilizing

AFM Skyrmions has recently been suggested [99–101]. At the core, the main differences in the material parameters between AFM and FM devices lies in the sign of the exchange interaction and the magnitude of the magnetostatic interaction. These differences have potentially large repercussions on the Thiele modeling of Skyrmions in the AFM systems. The negative exchange interaction leads to a vanishing gyrovector  $G = 0$ , implying two important consequences. First, the AFM Skyrmion always has zero transverse velocity relative to the direction of current flow. This, in FM Skyrmions, is true exclusively in the singular scenario  $\alpha = \eta$ . Second, and most importantly, a vanishing gyrovector implies a larger diffusion constant (7) and, consequently, smaller correlations (14). Depending on the value of the damping constant  $\alpha$  in the materials employed ( $\alpha \sim 0.01-1$ ), the difference in magnitude of the diffusion constants in FM and AFM skyrmions can easily span an order-of-magnitude difference. The magnitude of the magnetostatic interaction also complements the AFM Skyrmion, as it may lead to the stabilization of much smaller, and more thermally sensitive, particles. For all of these reasons, one expects that AFM Skyrmions would allow operation of our proposed device at higher currents and faster speeds.

Any undesired particle nucleation or annihilation taking place in the chambers does not influence the outgoing signal's  $p$  value as long as its rate remains proportional to the total number of Skyrmions present in each chamber. This proportionality is guaranteed for accidental particle annihilations, as it depends on how many Skyrmions are present in the chamber at any given time. Nucleations, on the other hand, can be potentially problematic for the device's proper functioning. Luckily, experimental observations of Skyrmions at room temperature seem to show no signs of thermally influenced Skyrmion instabilities. This notion leaves the interactions with material defects and background inhomogeneities [102] as the only other potential source of Skyrmion annihilations. As long as both chambers are similarly constructed, however, this leads to a similar rate of annihilations in both chambers, thus preserving input-to-output  $p$  values modulo a possible decrease in the output signal's frequency.

Overall, given the dc current driving the device (and possibly nucleating the necessary Skyrmions, as in Ref. [79]), we expect the Skyrmion reshuffler to operate at very low energies (on the order of microwatts). A more accurate metric would involve calculating the energy cost per reshuffled *bit* of information being transmitted through the telegraph signal. Typical CMOS-based solutions reshuffle clocked stochastic bitstreams [76] whose energy consumption can be estimated at approximately 10 pJ/bit. Placing their large area imprint problems aside, they are expected to perform efficiently only for slow bitstreams, as their energy consumption scales linearly with the signal's frequency. On the other hand, our Skyrmion reshuffler

constant energy costs will prove ideal for reshuffling high-frequency streams instead. As already mentioned, the device modeled in this section considered a constant Skyrmion injection rate of 0.2 nucleations/ns, thus allowing us to potentially reshuffle signals with frequencies as high as 5 GHz, resulting in an equivalent energy-per-bit cost of 5 fJ/bit, which is orders of magnitude lower.

## V. SKYRMION NEURON

We now turn to demonstrate how a similar design can be used to emulate the behavior of a neuron. Neural functioning relies on the ability to transmit and receive electrochemical signals to and from a large number of interconnected neurons by means of its *dendritic* connections (see Fig. 11). As coupled neurons spike, the receiving neuron registers the event with a voltage increase (or decrease) across its cellular membrane. The underlying physical mechanism for this behavior is the presence of ion channels scattered over the cell's membrane responsible for these potential differences. Such physical channels are not ideal, however, and *leak* over time, resulting in a steady decay of the neuron's voltage towards its resting potential in the absence of incoming electrochemical pulses. As a result of this behavior, a neuron can be thought of as a leaky capacitor.

If incoming neuronal activity is registered at a high enough frequency, however, the receiving neuron overcomes its leaking voltage and steadily charges. A threshold potential exists beyond which the neuron suddenly discharges and resets. This basic model of neuronal functioning is known as the *leaky integrate-and-fire* neuron model [103,104]. The neuron effectively serves as a basic memory integrating the sum of past voltage spikes received, with the added property that this memory is lost over time if a potential threshold is not reached.

The analogies to our Skyrmion reshuffler are already apparent, as the injection of particles into it can be thought of as a response to a voltage spike train (shown in Fig. 3). In

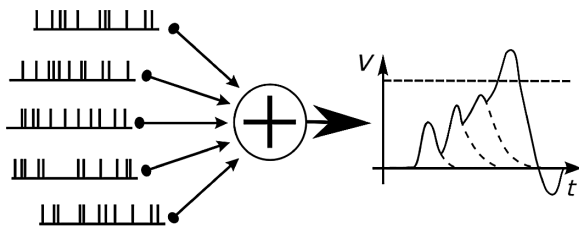


FIG. 11. A neuron collects neuronal spiking activity from nearby neurons. The incoming spikes lead to an increasing voltage potential between the inside and outside of the receiving neuron. Once the potential difference reaches a certain threshold, the receiving neuron discharges by releasing a voltage spike to its axon terminals, where the signal is transmitted through synapses to other neurons. Because of voltage leakage across the cell membrane, the neuron can be thought of as a leaky capacitor with low breakdown voltage.

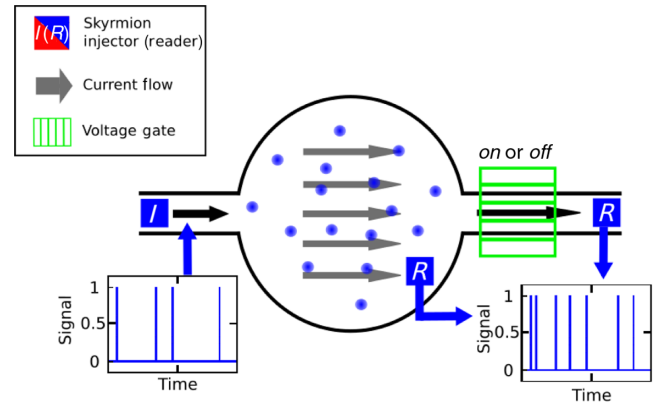


FIG. 12. The Skyrmion neuron consists of a magnetic chamber into which Skyrmions are injected depending on the state of one or multiple input telegraph noise signals. A voltage gate, initially in an *on* state, impedes the Skyrmions from drifting to the output conduit, thus leading to particle accumulation. A reading element placed inside the chamber can be used to estimate the Skyrmion density inside the chamber and switch off the voltage gate when a critical density is reached.

this sense, the collecting of Skyrmions inside the chambers serves as a history of the input spike train. If the passage of Skyrmions through the output conduit are to be precluded (such as with a voltage gate [35,105]), Skyrmions progressively accumulate inside the geometry, where their density can be estimated via a reading element placed inside each chamber (see Fig. 12). Each chamber can then be thought of as a reservoir collecting the memory of whatever input signal is employed to populate it.

Furthermore, an upper limit exists to how many Skyrmions may be crammed into each such chamber. In fact, as Skyrmions become compressed with their neighbors to length scales comparable to the typical Skyrmion diameter, the combination of dipolar strain among particles with thermal effects breaking topological stability may cause them to annihilate. The topological stability of the Skyrmion profile is only guaranteed under continuous deformations of the magnetic texture [24,106]. The introduction of a sufficiently large thermal field in the magnetization dynamics can make a Skyrmion collapse with some probability [14,107–111]. Alternatively, and possibly more importantly, Skyrmion annihilation can be biased by the presence of randomly scattered material defects in the magnetic sample populated by the Skyrmions. As such, small room-temperature Skyrmions can potentially annihilate (and nucleate) simply due to thermal fluctuations and material disorders. The maximal particle density inside a chamber can hence be thought of as a saturation threshold beyond which memory of the input signal will certainly be destroyed.

In Fig. 13, we perform micromagnetic simulations at 300 K to establish the maximal number of approximately 39-nm Skyrmions which can be stabilized inside chambers of varying sizes. We nucleate the Skyrmions randomly in

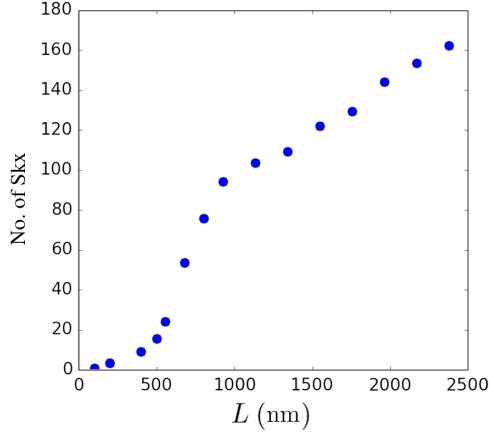


FIG. 13. Maximum number of approximately 39-nm Skyrmions that can be stabilized in a circular chamber as a function of chamber diameter at 300 K.

the chamber in ever-increasing numbers and allow the magnetic texture to stabilize for 2 ns before we count the remaining Skyrmions. This process is then repeated ten times before computing the average. For each chamber diameter explored, a saturation value is found beyond which no more Skyrmions can be added reliably into the geometry.

The combination of memory due to particle conservation and memory loss from annihilations allows one to view our proposed Skyrmionic chamber as a lossy memory storage device which integrates an incoming signal while allowing a certain decay of the accumulated information. Upon switching off the voltage gate, the collected Skyrmions can be released into the output conduit whenever a certain threshold Skyrmion density is reached (as measured by a reading element inside the chamber). Following these principles, the functioning of our device behaves as a leaky integrate-and-fire neuron where, instead of integrating discrete current pulses through electric potential accumulation before discharging, our device collects Skyrmions instead and successively dumps them into the output conduit.

## VI. METHODS

The three-dimensional micromagnetic simulations are performed using the MuMAX3 graphics processing unit (GPU)-accelerated micromagnetic simulation program [112]. The average energy density contains the exchange energy, the anisotropy energy, the applied field (Zeeman) energy, the magnetostatic (demagnetization) energy and the DMI energy terms. In all simulations, the thickness of the magnetic nanotracks is 2 nm. The length of the input-output conduits is 50 nm, while the width is set to 100 nm. The magnetic parameters used in the simulations are saturation magnetization,  $M_S = 1200$  kA/m; exchange stiffness,  $A_{\text{ex}} = 8$  pJ/m; interface-induced DMI constant,

$D = 2.1$  mJ/m<sup>2</sup>; perpendicular magnetic anisotropy constant,  $K_u = 0.9$  MJ/m<sup>3</sup>; and gyromagnetic ratio,  $\gamma = -2.211 \times 10^5$  m/A s. The Gilbert damping coefficient  $\alpha$  is set to 0.1. The choice of these values is consistent with interfacially stabilized Skyrmions on Pt/Co/MgO nanostructures [18].

All models are discretized into tetragonal cells with a constant cell size of  $2 \times 2 \times 2$  nm<sup>3</sup> in the simulations, whose linear size is smaller than both the fundamental length scale  $A_{\text{ex}}/D \simeq 4$  nm and the domain-wall width  $\sqrt{A_{\text{ex}}/K_u} \simeq 3$  nm. With these parameters, we observe the stabilization of Skyrmions with an average of diameter of about 39 nm at both zero and 300-K temperatures. The integration time steps used are  $5 \times 10^{-12}$  s and  $5 \times 10^{-14}$  s at 0 and 300 K, respectively. At finite temperatures, breathing modes are observed at gigahertz frequencies. Owing to the large Skyrmion sizes relative to the fundamental length scales, the Skyrmion stabilities observed are not an artifact of the small mesh sizes used and the general continuum approximation of the micromagnetic modeling.

The tracking of Skyrmion particles is performed on dynamical snapshots taken at each time step using the PYTHON implementation of the DLIB open-source machine learning library [113]. The classic histogram of oriented gradients feature combined with the linear classifier, the image pyramid, and the sliding window detection scheme are used to train a detector to recognize Skyrmions using a training set of 200 stabilized Skyrmion profiles. From the geometry's total magnetization profile, the tracking scheme allows us to obtain a set of regions containing one Skyrmion each only.

The computation of the Skyrmion center is performed by first fitting the magnetic profile of each region with a cubic spline interpolation and then finding the maximum  $z$  component of the magnetization on the interpolated profile. The algorithm allows for resolution of the Skyrmion center of about a picometer. The gyrotropic parameters are computed by performing the relevant surface integrals on the interpolated profile of each Skyrmion particle, as discussed in Eqs. (3) and (4).

The  $n$ -body Thiele dynamics are solved using a specialized GPU-accelerated CUDA C++ solver developed by the authors. The stochastic dynamical system of equations is solved employing a Heun scheme ensuring convergence to the proper Stratonovich solution. The current-density distributions are first obtained by simulating the current flow using COMSOL [114] for the geometry discussed. Room-temperature Skyrmions are known to exhibit breathing modes [87]; these modes will, however, not impact the net dynamics due to the gyrotropic terms being effectively scale-free in the particle size [86] when the Skyrmion size is much larger than the domain-wall width  $\sqrt{A_{\text{ex}}/K_u} \simeq 4.35$  nm. Qualitatively different dynamical behavior can, however, be expected for large Skyrmions, where an extra mass term is expected to play a role in the

Thiele description. For the material parameters in question, the numerical fitting constants for the Skyrmion-Skyrmion two-body repulsions are found to be  $\mathbf{a} \simeq [2.709, -5.643, 0.964]$ , whereas the fitting constants for boundary repulsions are  $\mathbf{b} \simeq [0.001419, -0.02631, 0.24135, -1.1609, 3.3547, -2.1786]$ . In this work, we take  $\eta = \alpha$  and  $\mu = 1$  for the sake of convenience.

## VII. DISCUSSION

The impracticality of performing complex micromagnetic simulations out to long timescales currently poses an obstacle to the design and proof of concept of alternative spintronic-based devices with a  $>$  micrometer area imprint. Under suitable simplifying assumptions, however, the behavior of solitonic magnetic spin-textures can be radically simplified and reduced to classical  $n$ -body problems, which can be tackled through a plethora of numerical techniques. We show in this paper how one such *particle* model (the Thiele equation) can be phenomenologically tuned in such a way to account for complex exchange and dipole-mediated interactions among stable magnetic Skyrmions. By means of the tools developed, we propose and model two Skyrmion devices whose behavior would be computationally intractable via standard micromagnetic techniques.

The Skyrmion reshuffler encodes a telegraph noise signal into a sequence of Skyrmions injected and current driven through two separate chambers. The dominance of thermal diffusion in each chamber scrambles the particle order in such a way that the output sequence can be used to reconstruct an output signal with negligible correlations to the input one. Through simple scaling analyses, we show how the system parameters impact these correlations and balance the trade-offs between speed and effectiveness of the device's operation. Leveraging the interplay between Skyrmion particle stability and thermal diffusivity, we argue that the Skyrmion reshuffler stands to solve a long-standing problem in the field of stochastic computing, where computations defined over stochastic signals require correlations to be absent for proper functioning. The spintronic basis of the Skyrmion reshuffler's design allows for highly attractive area imprint and energy costs.

The Skyrmion neuron adapts the Skyrmion reshuffler's design to propose a device capable of emulating the integrate-and-fire characteristics of a neuron. By means of an added voltage gate selectively prohibiting the outflow of Skyrmions from the chamber, as well as an extra readout element *inside* the chamber, the Skyrmion density in the chamber can be measured and the voltage gate released upon a certain threshold being reached. In doing so, the chamber integrates the signal intensity (or length) driving the input sequence of Skyrmions injected into the chamber. To complete the analogy with the animal neuron, we argue that Skyrmions perform the role of both voltage accumulation and neurotransmitters in this specific layout. The

devices we propose are compatible with a standard CMOS and can also be the building block of future fully spintronic probabilistic computers.

Overall, the sensitivity of magnetic soliton structures to small driving currents and thermal noise makes them optimal candidates for the development of alternative probabilistic devices. Furthermore, the *nanoscale* size of these particles implicitly guarantees that devices employing them will be both energy efficient and scalable. Our results suggest that the basic research currently being done on these exotic magnetic solitons fertilizes the field for future disruptive applications.

## ACKNOWLEDGMENTS

This work was funded by European FET OPEN ‘‘Bambi’’ Project No. 618024 and European Research Council (ERC) ‘‘bioSPINspired’’ Grant No. 682955. J.-V. K. and V. C. acknowledge support from the Horizon2020 Framework Programme of the European Commission (Project No. H2020-FETOPEN-2014-2015-RIA) under Contract No. 665095 (MAGicSky). The authors would like to thank A. Thiaville for his very useful comments during the revision of the manuscript.

## APPENDIX A: QUALITATIVE INFLUENCE OF DIPOLE EFFECTS ON SKYRMION REPULSION IN THE ULTRATHIN-FILM LIMIT

A magnetic texture  $\mathbf{M} = \mathbf{M}(x, y, z)$  with a constant magnetic saturation  $|\mathbf{M}| = M_S$  extended over a three-dimensional domain  $\Omega$  of thickness  $d$  can be described by a micromagnetic free energy which, in the presence of an out-of-plane uniaxial anisotropy (along the  $z$  axis) and an interfacial DMI, takes the form [115,116]

$$E_M = \frac{A}{M_S^2} \int_{\Omega} d^3r |\nabla \mathbf{M}|^2 + \frac{K}{M_S^2} \int_{\Omega} d^3r |M_z|^2 \quad (\text{A1})$$

$$+ \mu_0 \int_{\Omega} \int_{\Omega} d^3r d^3r' \frac{\nabla \cdot \mathbf{M}(\mathbf{r}) \nabla \cdot \mathbf{M}(\mathbf{r}')}{8\pi |\mathbf{r} - \mathbf{r}'|} \quad (\text{A2})$$

$$+ \frac{Dd}{M_S^2} \int \int dx dy \mathbf{M} \cdot (\partial_x \mathbf{M} \times \partial_y \mathbf{M}), \quad (\text{A3})$$

where  $A$ ,  $K$ , and  $D$  are the exchange stiffness, the anisotropy, and the Dzyaloshinskii-Moriya strength, respectively. In order of appearance, the terms in the magnetic free energy are the exchange term, which prefers constant magnetization configurations; the magnetocrystalline anisotropy, which favors out-of-plane magnetization configurations; the magnetostatic term, which prefers

divergence-free configurations; and the surface DMI term, which favors chiral symmetry breaking.

In the limit of ultrathin ferromagnetic films where the sample thickness is smaller than the exchange length  $l_{\text{ex}}$  [ $d \leq l_{\text{ex}} = \sqrt{2A/(\mu_0 M_S^2)}$ ], the magnetic free energy above can be described by a model where the stray-field energy is expressed as a local shape anisotropy term [117,118]. This model can, in turn, be used to treat the simplified one-dimensional case of magnetic wires in the presence of the DMI, with the magnetic energy given by [119]

$$E_{\text{M}} = \int_{-\infty}^{\infty} dx [|\partial_x \theta|^2 + Q^2 \sin^2 \theta] - \kappa \pi, \quad (\text{A4})$$

where  $\kappa = D\sqrt{[2/(\mu_0 M_S^2 A)]}$ ,  $Q = \sqrt{[(2K)/(\mu_0 M_S^2)] - 1}$ , and the magnetic profile is parametrized as  $\mathbf{M} = M_S(\sin \theta, 0, \cos \theta)$ . The dimensionless constant  $Q$ , known as the *quality factor*, captures both the contributions of the crystalline anisotropy and the stray field in the ultrathin-film limit considered. The energy is minimized by domain-wall solutions whose explicit form can be verified to be

$$\theta(x) = 2 \arctan[e^{-Qx}]. \quad (\text{A5})$$

Let us then consider a magnetic texture consisting of two such domain walls separated by a distance  $\delta$ :

$$\begin{aligned} \theta(x) &= \theta_+(x) + \theta_-(x) \\ &= 2 \arctan[\eta e^{Qx}] + 2 \arctan[\eta e^{-Qx}], \end{aligned} \quad (\text{A6})$$

with  $\eta = \exp(-Q\delta/2)$ . The total energy of the system can be written as

$$E_{\theta} = E_{\theta_+} + E_{\theta_-} + E_{\theta_+, \theta_-}^{\text{int}}(\delta), \quad (\text{A7})$$

$$\begin{aligned} E_{\theta_+, \theta_-}^{\text{int}}(\delta) &= \int_{-\infty}^{\infty} dx \left[ \partial_x \theta_+ \partial_x \theta_- \right. \\ &\quad \left. + \frac{1}{2} \sin 2\theta_+ \sin 2\theta_- - 2 \sin^2 \theta_+ \sin^2 \theta_- \right], \end{aligned} \quad (\text{A8})$$

where the first two terms are simply the minimum energy of each domain wall taken independently, while the third measures the interaction potential of the two walls. The repulsive force between the two domain walls is then straightforwardly given by the derivative of interaction potential with respect to the distance separating the walls [ $F_{\theta_+, \theta_-}(\delta) = -\partial_{\delta} E_{\theta_+, \theta_-}^{\text{int}}$ ]. Tedious, but fairly elemental, analysis then results in the following repulsion force:

$$\begin{aligned} F_{\theta_+, \theta_-}(\delta) &= 2Q\eta^2(I_{1,1,1,0} - 4I_{1,1,1,2}) \\ &\quad + 2^5 \eta^4(2I_{2,2,1,0} - I_{3,1,0,1}), \end{aligned} \quad (\text{A9})$$

$$I_{Q,R,S,T} = \int_0^{\infty} \frac{ds}{s} s^{-(b-a)} \frac{[1 - (\frac{a}{s})^2]^T [1 - (\eta s)^2]^S}{[1 + (\frac{a}{s})^2]^{R+T} [1 + (\eta s)^2]^{Q+R}}. \quad (\text{A10})$$

The repulsion force is effectively dominated by the behavior of the powers of  $\eta$  appearing in the prefactors. As such, the repulsive force can be expected to decay exponentially in the distance  $\delta$  between the two domain walls. This result is a direct consequence of the ultrathin-film limit, which allows one to write the magnetic stray field as an effective shape anisotropy and is not expected to qualitatively change for the case of two-dimensional magnetic Skyrmions considered in the main text.

## APPENDIX B: SKYRMION PROPERTIES UNDER DIFFERENT MATERIAL CONDITIONS

In this section, we list all of the material parameters explored throughout our micromagnetic simulations. In order to perform our analysis of the Skyrmion-Skyrmion repulsive forces in the main text, we require that the micromagnetically simulated magnetic textures relax to their stable values within short enough timescales such that all further dynamical behavior can be considered *physically relevant*. The seven sets of material values shown in Tables I and II and Figs. 14–20 are named S1–S7 (S2 corresponds to the results presented in the main text).

TABLE I. Material parameters.

	$M_S$ (MA/m)	$J_{\text{ex}}$ (fJ/m)	$D$ (mJ/m <sup>2</sup> )	$K$ (MJ/m <sup>3</sup> )	$B$ (mT)	$R_{\text{Skx}}$ (nm)
S1	1.4	27.5	2.05	1.45	0	23.2
S2	1.45	27.5	2.05	1.45	20	19.1
S3	1.4	27.5	2.6	1.45	20	30.3
S4	1.4	27.5	2.6	1.60	-15	14.9
S5	1.5	25.0	2.4	1.60	30	27.9
S6	1.0	5.0	2.05	0.9	150	11.9
S7	1.2	8.0	2.1	0.9	150	14.9

TABLE II. Skyrmion (Skx)-Skx repulsion.

	$ F  \propto \exp\{-[(a_2 d^2 + a_1 d + a_0)/(1+d)]\}$		
	$a_2$	$a_1$	$a_0$
S1	1.245	1.249	-3.449
S2	2.709	-5.643	0.964
S3	2.488	-1.899	-2.676
S4	1.13	2.171	-6.623
S5	2.219	-1.159	-3.358
S6	0.059	10.757	-16.738
S7	0.766	5.452	-11.894

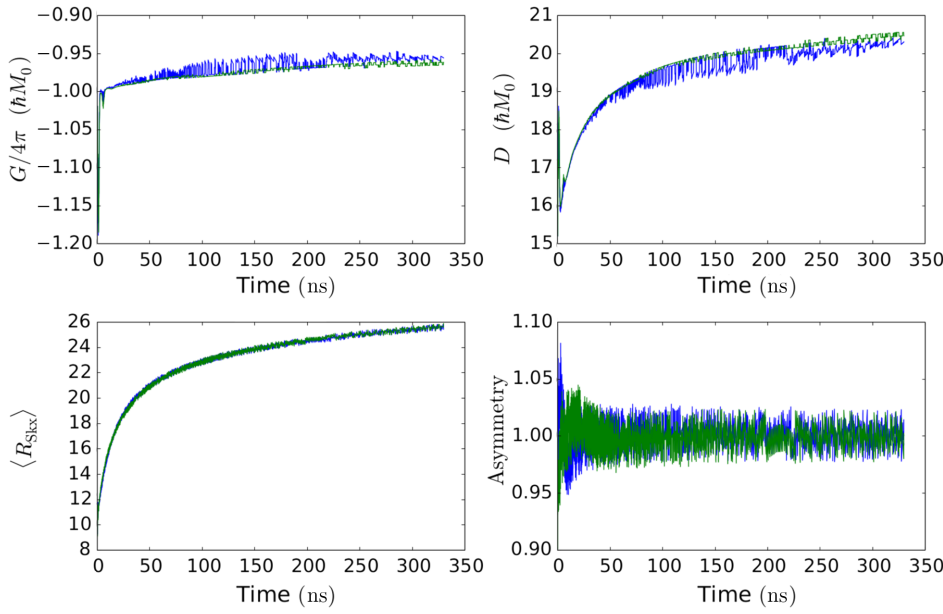


FIG. 14. Topological charge, damping, average radius, and asymmetry observed through micromagnetic simulations of two repelling skyrmions via the material parameter set *S1*.

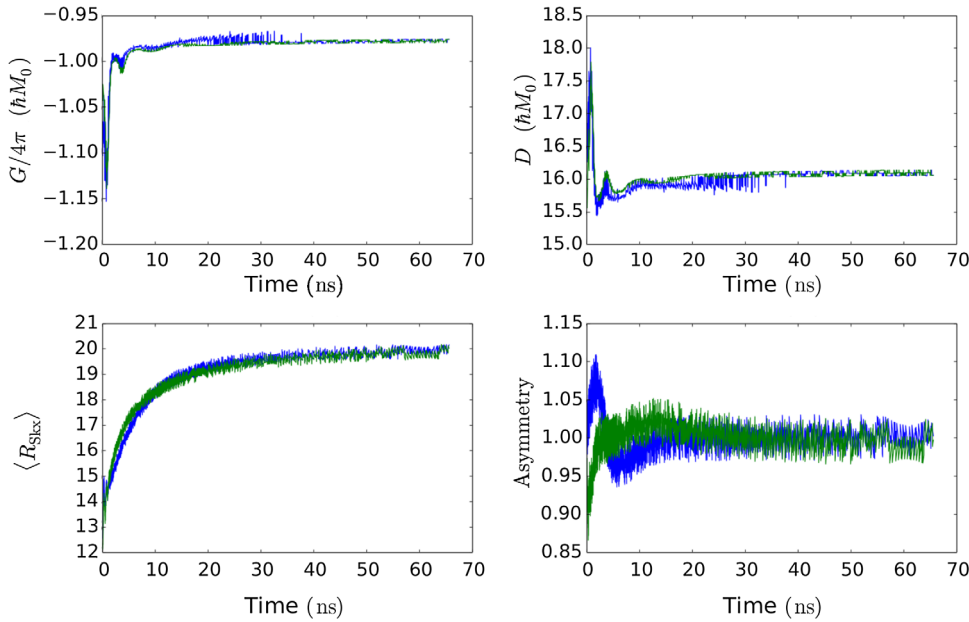


FIG. 15. Topological charge, damping, average radius, and asymmetry observed through micromagnetic simulations of two repelling Skyrmions via the material parameter set *S2*.

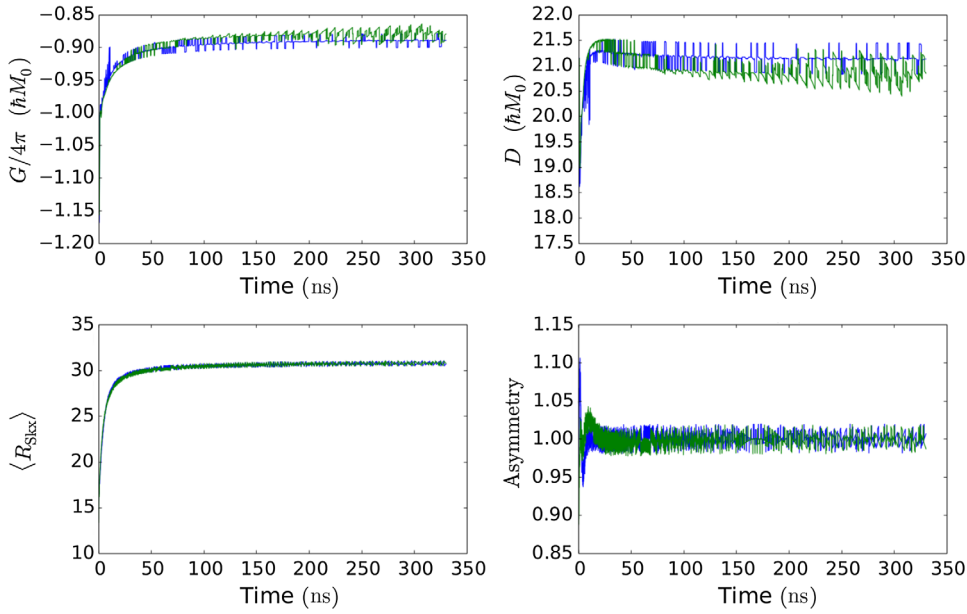


FIG. 16. Topological charge, damping, average radius, and asymmetry observed through micromagnetic simulations of two repelling Skyrmions via the material parameter set S3.

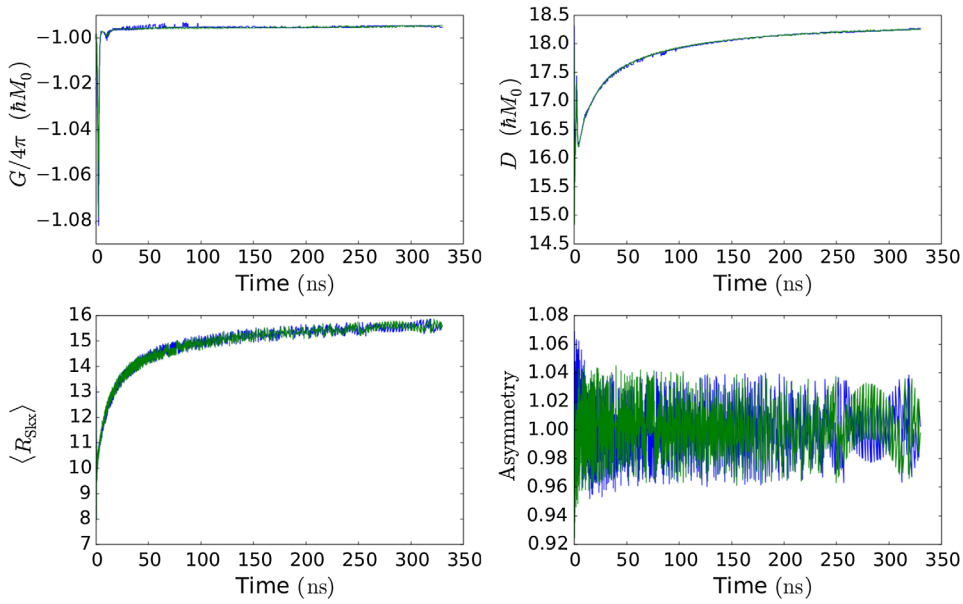


FIG. 17. Topological charge, damping, average radius, and asymmetry observed through micromagnetic simulations of two repelling Skyrmions via the material parameter set S4.

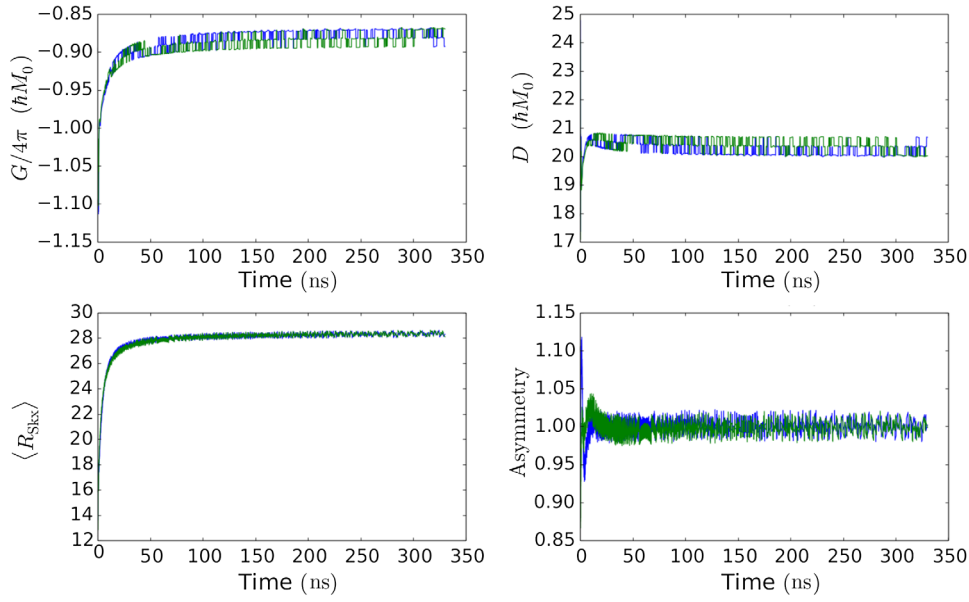


FIG. 18. Topological charge, damping, average radius, and asymmetry observed through micromagnetic simulations of two repelling Skyrmions via the material parameter set S5.

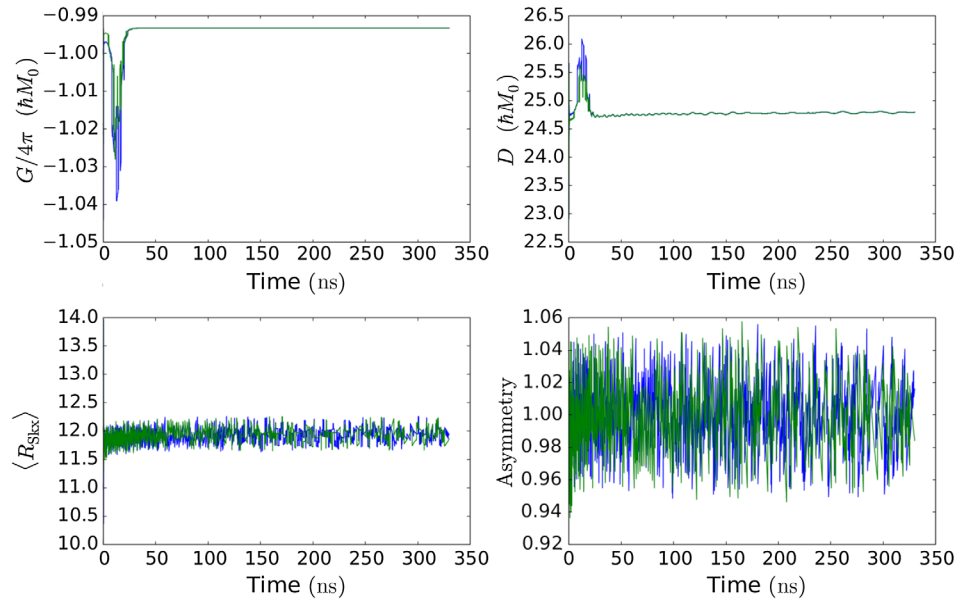


FIG. 19. Topological charge, damping, average radius, and asymmetry observed through micromagnetic simulations of two repelling Skyrmions via the material parameter set S6.

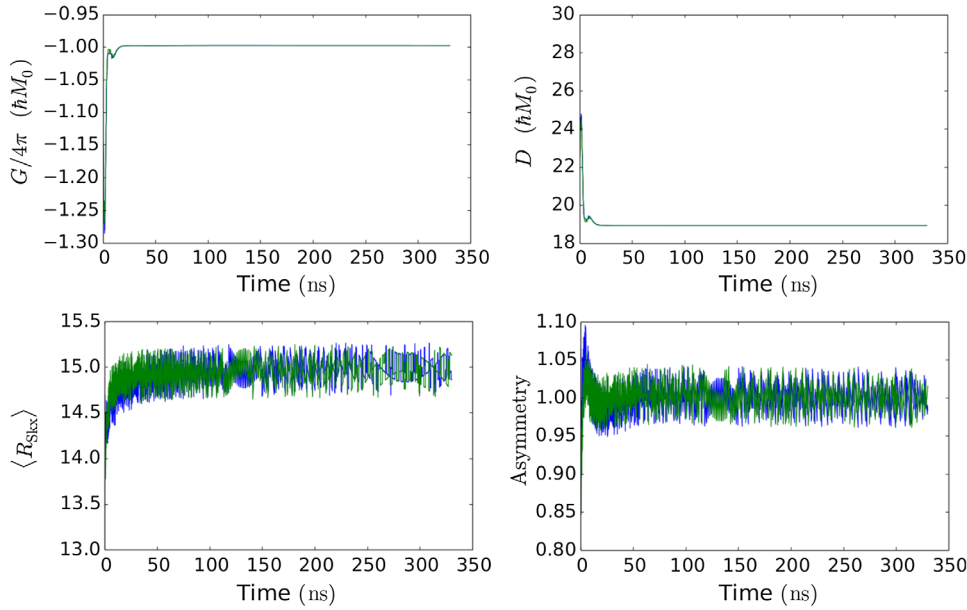


FIG. 20. Topological charge, damping, average radius, and asymmetry observed through micromagnetic simulations of two repelling Skyrmions via the material parameter set *S7*.

- [1] A. Fert, V. Cros, and J. Sampaio, Skyrmions on the track, *Nat. Nanotechnol.* **8**, 152 (2013).
- [2] N. Nagaosa and Y. Tokura, Topological properties and dynamics of magnetic Skyrmions, *Nat. Nanotechnol.* **8**, 899 (2013).
- [3] J. Sampaio, V. Cros, S. Rohart, A. Thiaville, and A. Fert, Nucleation, stability and current-induced motion of isolated magnetic Skyrmions in nanostructures, *Nat. Nanotechnol.* **8**, 839 (2013).
- [4] J. Iwasaki, M. Mochizuki, and N. Nagaosa, Universal current-velocity relation of Skyrmion motion in chiral magnets, *Nat. Commun.* **4**, 1463 (2013).
- [5] X. Zhang, M. Ezawa, and Y. Zhou, Magnetic Skyrmion logic gates: Conversion, duplication and merging of Skyrmions, *Sci. Rep.* **5**, 9400 (2015).
- [6] W. Koshibae, Y. Kaneko, J. Iwasaki, M. Kawasaki, Y. Tokura, and N. Nagaosa, Memory functions of magnetic Skyrmions, *Jpn. J. Appl. Phys.* **54**, 053001 (2015).
- [7] A. Fert, N. Reyren, and V. Cros, Magnetic Skyrmions: Advances in physics and potential applications, *Nat. Rev. Mater.* **2**, 17031 (2017).
- [8] A. Neubauer, C. Pfleiderer, B. Binz, A. Rosch, R. Ritz, P. G. Niklowitz, and P. Böni, Topological Hall Effect in the A Phase of MnSi, *Phys. Rev. Lett.* **102**, 186602 (2009).
- [9] C. Pappas, E. Lelièvre-Berna, P. Falus, P. M. Bentley, E. Moskvin, S. Grigoriev, P. Fouquet, and B. Farago, Chiral Paramagnetic Skyrmion-like Phase in MnSi, *Phys. Rev. Lett.* **102**, 197202 (2009).
- [10] A. Tonomura, X. Yu, K. Yanagisawa, T. Matsuda, Y. Onose, N. Kanazawa, H. S. Park, and Y. Tokura, Real-space observation of Skyrmion lattice in helimagnet MnSi thin samples, *Nano Lett.* **12**, 1673 (2012).
- [11] X. Yu, Y. Onose, N. Kanazawa, J. Park, J. Han, Y. Matsui, N. Nagaosa, and Y. Tokura, Real-space observation of a two-dimensional Skyrmion crystal, *Nature (London)* **465**, 901 (2010).
- [12] S. X. Huang and C. L. Chien, Extended Skyrmion Phase in Epitaxial FeGe(111) Thin Films, *Phys. Rev. Lett.* **108**, 267201 (2012).
- [13] S. Heinze, K. Von Bergmann, M. Menzel, J. Brede, A. Kubetzka, R. Wiesendanger, G. Bihlmayer, and S. Blügel, Spontaneous atomic-scale magnetic Skyrmion lattice in two dimensions, *Nat. Phys.* **7**, 713 (2011).
- [14] N. Romming, C. Hanneken, M. Menzel, J. E. Bickel, B. Wolter, K. von Bergmann, A. Kubetzka, and R. Wiesendanger, Writing and deleting single magnetic Skyrmions, *Science* **341**, 636 (2013).
- [15] W. Jiang, P. Upadhyaya, W. Zhang, G. Yu, M. B. Jungfleisch, F. Y. Fradin, J. E. Pearson, Y. Tserkovnyak, K. L. Wang, O. Heinonen *et al.*, Blowing magnetic Skyrmion bubbles, *Science* **349**, 283 (2015).
- [16] C. Moreau-Luchaire, C. Moutafis, N. Reyren, J. Sampaio, C. Vaz, N. Van Horne, K. Bouzehouane, K. Garcia, C. Deranlot, P. Warnicke *et al.*, Additive interfacial chiral interaction in multilayers for stabilization of small individual Skyrmions at room temperature, *Nat. Nanotechnol.* **11**, 444 (2016).
- [17] S. Woo, K. Litzius, B. Krüger, M.-Y. Im, L. Caretta, K. Richter, M. Mann, A. Krone, R. M. Reeve, M. Weigand *et al.*, Observation of room-temperature magnetic Skyrmions and their current-driven dynamics in ultrathin metallic ferromagnets, *Nat. Mater.* **15**, 501 (2016).
- [18] O. Boulle, J. Vogel, H. Yang, S. Pizzini, D. de Souza Chaves, A. Locatelli, T. O. Menteş, A. Sala, L. D. Buda-Prejbeanu, O. Klein *et al.*, Room-temperature chiral magnetic Skyrmions in ultrathin magnetic nanostructures, *Nat. Nanotechnol.* **11**, 449 (2016).
- [19] F. Jonietz, S. Mühlbauer, C. Pfleiderer, A. Neubauer, W. Münzer, A. Bauer, T. Adams, R. Georgii, P. Böni, R. Duine *et al.*, Spin transfer torques in MnSi at ultralow current densities, *Science* **330**, 1648 (2010).

- [20] X. Yu, N. Kanazawa, W. Zhang, T. Nagai, T. Hara, K. Kimoto, Y. Matsui, Y. Onose, and Y. Tokura, Skyrmion flow near room temperature in an ultralow current density, *Nat. Commun.* **3**, 988 (2012).
- [21] W. Jiang, X. Zhang, G. Yu, W. Zhang, M. B. Jungfleisch, J. E. Pearson, O. Heinonen, K. L. Wang, Y. Zhou, A. Hoffmann *et al.*, Direct observation of the Skyrmion Hall effect, *Nat. Phys.* **13**, 162 (2017).
- [22] A. Hrabec, J. Sampaio, M. Belmeguenai, I. Gross, R. Weil, S. M. Chérif, A. Stachkevitch, V. Jacques, A. Thiaville, and S. Rohart, Current-induced Skyrmion generation and dynamics in symmetric bilayers, *Nat. Commun.* **8**, 15765 (2017).
- [23] K. Litzius, I. Lemesch, B. Krüger, P. Bassirian, L. Caretta, K. Richter, F. Büttner, K. Sato, O. A. Tretiakov, J. Förster *et al.*, Skyrmion Hall effect revealed by direct time-resolved x-ray microscopy, *Nat. Phys.* **13**, 170 (2017).
- [24] A. N. Bogdanov and U. K. Röbber, Chiral Symmetry Breaking in Magnetic Thin Films and Multilayers, *Phys. Rev. Lett.* **87**, 037203 (2001).
- [25] J. Iwasaki, M. Mochizuki, and N. Nagaosa, Current-induced Skyrmion dynamics in constricted geometries, *Nat. Nanotechnol.* **8**, 742 (2013).
- [26] S.-Z. Lin, C. Reichhardt, C. D. Batista, and A. Saxena, Particle model for Skyrmions in metallic chiral magnets: Dynamics, pinning, and creep, *Phys. Rev. B* **87**, 214419 (2013).
- [27] C. Reichhardt, D. Ray, and C. J. Olson Reichhardt, Collective Transport Properties of Driven Skyrmions with Random Disorder, *Phys. Rev. Lett.* **114**, 217202 (2015).
- [28] J. Müller and A. Rosch, Capturing of a magnetic Skyrmion with a hole, *Phys. Rev. B* **91**, 054410 (2015).
- [29] X. Zhang, G. Zhao, H. Fangohr, J. P. Liu, W. Xia, J. Xia, and F. Morvan, Skyrmion-Skyrmion and Skyrmion-edge repulsions in Skyrmion-based racetrack memory, *Sci. Rep.* **5**, 7643 (2015).
- [30] Y. Tchoe and J. H. Han, Skyrmion generation by current, *Phys. Rev. B* **85**, 174416 (2012).
- [31] W. Legrand, D. Maccariello, N. Reyren, K. Garcia, C. Moutafis, C. Moreau-Luchaire, S. Collin, K. Bouzehouane, V. Cros, and A. Fert, Room-temperature current-induced generation and motion of sub-100 nm Skyrmions, *Nano Lett.* **17**, 2703 (2017).
- [32] Y. Zhou and M. Ezawa, A reversible conversion between a Skyrmion and a domain-wall pair in a junction geometry, *Nat. Commun.* **5**, 4652 (2014).
- [33] R. Tomasello, E. Martinez, R. Zivieri, L. Torres, M. Carpentieri, and G. Finocchio, A strategy for the design of Skyrmion racetrack memories, *Sci. Rep.* **4**, 6784 (2014).
- [34] S. Mühlbauer, B. Binz, F. Jonietz, C. Pfleiderer, A. Rosch, A. Neubauer, R. Georgii, and P. Böni, Skyrmion lattice in a chiral magnet, *Science* **323**, 915 (2009).
- [35] W. Kang, Y. Huang, C. Zheng, W. Lv, N. Lei, Y. Zhang, X. Zhang, Y. Zhou, and W. Zhao, Voltage controlled magnetic Skyrmion motion for racetrack memory, *Sci. Rep.* **6**, 23164 (2016).
- [36] X. Zhang, Y. Zhou, M. Ezawa, G. Zhao, and W. Zhao, Magnetic Skyrmion transistor: Skyrmion motion in a voltage-gated nanotrack, *Sci. Rep.* **5**, 11369 (2015).
- [37] Y. Huang, W. Kang, X. Zhang, Y. Zhou, and W. Zhao, Magnetic Skyrmion-based synaptic devices, *Nanotechnology* **28**, 08LT02 (2017).
- [38] J. E. Miltat and M. J. Donahue, Numerical micromagnetics: Finite difference methods, in *Handbook of Magnetism and Advanced Magnetic Materials*, edited by H. Kronmüller and S. Parkin (Wiley InterScience, Hoboken, NJ, 2007).
- [39] G. D. Smith, *Numerical Solution of Partial Differential Equations: Finite Difference Methods* (Oxford University Press, New York, 1985).
- [40] I. Basheer and M. Hajmeer, Artificial neural networks: Fundamentals, computing, design, and application, *Journal of microbiological methods* **43**, 3 (2000).
- [41] D. Colliaux, P. Bessièrre, and J. Droulez, Cell signaling as a probabilistic computer, *International Journal of Approximate Reasoning* **83**, 385 (2017).
- [42] J. Von Neumann and R. Kurzweil, *The Computer and the Brain* (Yale University Press, New Haven, CT, 2012).
- [43] A. Thiele, Steady-State Motion of Magnetic Domains, *Phys. Rev. Lett.* **30**, 230 (1973).
- [44] A. N. Burkitt, A review of the integrate-and-fire neuron model: I. Homogeneous synaptic input, *Biol. Cybern.* **95**, 1 (2006).
- [45] T. Rao, *Error Coding for Arithmetic Processors* (Academic, New York, 1974).
- [46] B. Pratt, M. Caffrey, J. F. Carroll, P. Graham, K. Morgan, and M. Wirthlin, Fine-grain SEU mitigation for FPGAs using partial TMR, *IEEE Trans. Nucl. Sci.* **55**, 2274 (2008).
- [47] I. Koren and C. M. Krishna, *Fault-Tolerant Systems* (Morgan Kaufmann, Burlington, MA, 2010).
- [48] B. R. Gaines, *Stochastic Computing* (Association for Computing Machinery, New York, 1967), p. 149.
- [49] A. Alaghi and J. P. Hayes, Survey of stochastic computing, *ACM Trans. Embedded Comput. Syst.* **12**, 92 (2013).
- [50] A. Morro, V. Canals, A. Oliver, M. L. Alomar, and J. L. Rossello, Ultra-fast data-mining hardware architecture based on stochastic computing, *PLoS One* **10**, e0124176 (2015).
- [51] V. Canals, A. Morro, A. Oliver, M. L. Alomar, and J. L. Rossello, A new stochastic computing methodology for efficient neural network implementation, *IEEE Trans. Neural Networks Learning Syst.* **27**, 551 (2016).
- [52] J. S. Friedman, L. E. Calvet, P. Bessièrre, J. Droulez, and D. Querlioz, Bayesian inference with Muller *c*-elements, *IEEE Trans. Circuits Syst. I* **63**, 895 (2016).
- [53] J. Von Neumann, Probabilistic logics and the synthesis of reliable organisms from unreliable components, *Autom. Stud.* **34**, 43 (1956).
- [54] S. Toral, J. Quero, and L. Franquelo, Stochastic pulse coded arithmetic, in *Proceedings of the 2000 IEEE International Symposium on Circuits and Systems (ISCAS 2000)*, Geneva, 2000 (IEEE, New York, 2000), p. 599.
- [55] W. Qian and M. D. Riedel, The synthesis of robust polynomial arithmetic with stochastic logic, in *Proceedings of the 45th ACM/IEEE Design Automation Conference (DAC 2008)*, Anaheim, 2008 (IEEE, New York, 2008), p. 648.

- [56] X. Li, W. Qian, M. D. Riedel, K. Bazargan, and D. J. Lilja, A reconfigurable stochastic architecture for highly reliable computing, in *Proceedings of the 19th ACM Great Lakes Symposium on VLSI, Braintree, MA, 2009* (Association for Computing Machinery, New York, 2009), p. 315.
- [57] W. Qian, X. Li, M. D. Riedel, K. Bazargan, and D. J. Lilja, An architecture for fault-tolerant computation with stochastic logic, *IEEE Trans. Comput.* **60**, 93 (2011).
- [58] P. Mars and H. McLean, High-speed matrix inversion by stochastic computer, *Electron. Lett.* **12**, 457 (1976).
- [59] D. Zhang and H. Li, A stochastic-based FPGA controller for an induction motor drive with integrated neural network algorithms, *IEEE Transactions on Industrial Electronics* **55**, 551 (2008).
- [60] R. C. Baumann, Radiation-induced soft errors in advanced semiconductor technologies, *Trans. Device Mater. Reliab.* **5**, 305 (2005).
- [61] M. Parhi, M. D. Riedel, and K. K. Parhi, Effect of bit-level correlation in stochastic computing, in *Proceedings of the 2015 IEEE Conference on Digital Signal Processing, Singapore, 2015* (IEEE, New York, 2015), p. 463.
- [62] S. W. Golomb *et al.*, *Shift Register Sequences* (Aegean Park Press, Walnut Creek, CA, 1982).
- [63] P. Gupta and R. Kumaresan, Binary multiplication with  $p$ - $n$  sequences, *IEEE Trans. Acoust., Speech, Signal Process.* **36**, 603 (1988).
- [64] J. Ohta, T. Tokuda, K. Kagawa, Y. Terasawa, M. Ozawa, T. Fujikado, and Y. Tano, Large-scale integration-based stimulus electrodes for retinal prosthesis, in *Artificial Sight*, edited by M. S. Humayun, J. D. Weiland, G. Chader, and E. Greenbaum, Biological and Medical Physics, Biomedical Engineering (Springer, New York, 2007), p. 151.
- [65] N. Locatelli, A. Mizrahi, A. Accioly, R. Matsumoto, A. Fukushima, H. Kubota, S. Yuasa, V. Cros, L. G. Pereira, D. Querlioz *et al.*, Noise-Enhanced Synchronization of Stochastic Magnetic Oscillators, *Phys. Rev. Applied* **2**, 034009 (2014).
- [66] R. Perricone, Y. Liu, A. Dingler, X. S. Hu, and M. Niemier, Design of stochastic computing circuits using nanomagnetic logic, *IEEE Trans. Nanotechnol.* **15**, 179 (2016).
- [67] D. Vodenicarevic, N. Locatelli, A. Mizrahi, J. S. Friedman, A. F. Vincent, M. Romera, A. Fukushima, K. Yakushiji, H. Kubota, S. Yuasa *et al.*, Low-Energy True Random Number Generation with Superparamagnetic Tunnel Junctions for Unconventional Computing, *Phys. Rev. Applied* **8**, 054045 (2017).
- [68] A. Sengupta, M. Parsa, B. Han, and K. Roy, Probabilistic deep spiking neural systems enabled by magnetic tunnel junction, *IEEE Trans. Electron Devices* **63**, 2963 (2016).
- [69] R. Faria, K. Y. Camsari, and S. Datta, Low-barrier nanomagnets as  $p$ -bits for spin logic, *IEEE Magn. Lett.* **8**, 4105305 (2017).
- [70] B. Sutton, K. Y. Camsari, B. Behin-Aein, and S. Datta, Intrinsic optimization using stochastic nanomagnets, *Sci. Rep.* **7**, 44370 (2017).
- [71] R. Venkatesan, S. Venkataramani, X. Fong, K. Roy, and A. Raghunathan, Spintastic: Spin-based stochastic logic for energy-efficient computing, in *Proceedings of the 2015 Design, Automation and Test in Europe Conference and Exhibition, Grenoble, 2015* (EDA Consortium, San Jose, 2015), p. 1575.
- [72] P. Jeavons, D. A. Cohen, and J. Shawe-Taylor, Generating binary sequences for stochastic computing, *IEEE Trans. Inf. Theory* **40**, 716 (1994).
- [73] A. Alaghi and J. P. Hayes, Exploiting correlation in stochastic circuit design, in *Proceedings of the 2013 IEEE 31st International Conference on Computer Design (ICCD), Asheville, 2013* (IEEE, New York, 2013), p. 39.
- [74] B. Moons and M. Verhelst, Energy-efficiency and accuracy of stochastic computing circuits in emerging technologies, *IEEE J. Emerging Sel. Top. Circuits Syst.* **4**, 475 (2014).
- [75] R. Manohar, Comparing stochastic and deterministic computing, *IEEE Comput. Archit. Lett.* **14**, 119 (2015).
- [76] S. S. Tehrani, C. Winstead, W. J. Gross, S. Mannor, S. L. Howard, and V. C. Gaudet, Relaxation dynamics in stochastic iterative decoders, *IEEE Trans. Signal Process.* **58**, 5955 (2010).
- [77] D. Pinna, J. Grollier, V. Cros, D. Querlioz, P. Bessi ere, and J. Droulez, Device for generating a random electrical signal and associated architecture, French Patent No. WO2017/198758 A1 (23 November 2017).
- [78] G. Yu, P. Upadhyaya, Q. Shao, H. Wu, G. Yin, X. Li, C. He, W. Jiang, X. Han, P. K. Amiri *et al.*, Room-temperature Skyrmion shift device for memory application, *Nano Lett.* **17**, 261 (2017).
- [79] K. Everschor-Sitte, M. Sitte, T. Valet, J. Sinova, and A. Abanov, Skyrmion production on demand by homogeneous dc currents, *New J. Phys.* **9**, 092001 (2016).
- [80] C. Hanneken, F. Otte, A. Kubetzka, B. Dup e, N. Romming, K. Von Bergmann, R. Wiesendanger, and S. Heinze, Electrical detection of magnetic Skyrmions by tunnelling non-collinear magnetoresistance, *Nat. Nanotechnol.* **10**, 1039 (2015).
- [81] K. Everschor, M. Garst, R. A. Duine, and A. Rosch, Current-induced rotational torques in the Skyrmion lattice phase of chiral magnets, *Phys. Rev. B* **84**, 064401 (2011).
- [82] D. J. Clarke, O. A. Tretiakov, G.-W. Chern, Ya. B. Bazaliy, and O. Tchernyshyov, Dynamics of a vortex domain wall in a magnetic nanostrip: Application of the collective-coordinate approach, *Phys. Rev. B* **78**, 134412 (2008).
- [83] O. A. Tretiakov and O. Tchernyshyov, Vortices in thin ferromagnetic films and the Skyrmion number, *Phys. Rev. B* **75**, 012408 (2007).
- [84] I. A. Ado, O. A. Tretiakov, and M. Titov, Microscopic theory of spin-orbit torques in two dimensions, *Phys. Rev. B* **95**, 094401 (2017).
- [85] E. G. Tveten, A. Qaiumzadeh, O. A. Tretiakov, and A. Brataas, Staggered Dynamics in Antiferromagnets by Collective Coordinates, *Phys. Rev. Lett.* **110**, 127208 (2013).
- [86] C. Sch utte, J. Iwasaki, A. Rosch, and N. Nagaosa, Inertia, diffusion, and dynamics of a driven Skyrmion, *Phys. Rev. B* **90**, 174434 (2014).
- [87] J.-V. Kim, F. Garcia-Sanchez, J. Sampaio, C. Moreau-Luchaire, V. Cros, and A. Fert, Breathing modes of confined Skyrmions in ultrathin magnetic dots, *Phys. Rev. B* **90**, 064410 (2014).
- [88] O. A. Tretiakov, D. Clarke, G.-W. Chern, Ya. B. Bazaliy, and O. Tchernyshyov, Dynamics of Domain Walls in Magnetic Nanostrips, *Phys. Rev. Lett.* **100**, 127204 (2008).

- [89] F. Büttner, C. Moutafis, M. Schneider, B. Krüger, C. Günther, J. Geilhufe, C. v. K. Schmising, J. Mohanty, B. Pfau, S. Schaffert *et al.*, Dynamics and inertia of Skyrmionic spin structures, *Nat. Phys.* **11**, 225 (2015).
- [90] G. Tatara, H. Kohno, and J. Shibata, Microscopic approach to current-driven domain wall dynamics, *Phys. Rep.* **468**, 213 (2008).
- [91] T. Schulz, R. Ritz, A. Bauer, M. Halder, M. Wagner, C. Franz, C. Pfleiderer, K. Everschor, M. Garst, and A. Rosch, Emergent electrodynamics of Skyrmions in a chiral magnet, *Nat. Phys.* **8**, 301 (2012).
- [92] F. Mertens, A. Bishop, P. Christiansen, M. Soerensen, and A. Scott, in *Nonlinear Science at the Dawn of the 21st Century*, edited by P. L. Christiansen, M. P. Soerensen, and A. C. Scott, Lecture Notes in Physics Vol. 542 (Springer, Berlin, 2000).
- [93] R. E. Troncoso and Á. S. Núñez, Brownian motion of massive Skyrmions in magnetic thin films, *Ann. Phys. (Amsterdam)* **351**, 850 (2014).
- [94] R. Rajaraman, *Solitons and Instantons* (Elsevier Science, Amsterdam, 1982).
- [95] S. Rohart and A. Thiaville, Skyrmion confinement in ultrathin film nanostructures in the presence of Dzyaloshinskii-Moriya interaction, *Phys. Rev. B* **88**, 184422 (2013).
- [96] M.-W. Yoo, V. Cros, and J.-V. Kim, Current-driven Skyrmion expulsion from magnetic nanostrips, *Phys. Rev. B* **95**, 184423 (2017).
- [97] R. A. Fisher, Frequency distribution of the values of the correlation coefficient in samples from an indefinitely large population, *Biometrika* **10**, 507 (1915).
- [98] J.-V. Kim and M.-W. Yoo, Current-driven Skyrmion dynamics in disordered films, *Appl. Phys. Lett.* **110**, 132404 (2017).
- [99] J. Barker and O. A. Tretiakov, Static and Dynamical Properties of Antiferromagnetic Skyrmions in the Presence of Applied Current and Temperature, *Phys. Rev. Lett.* **116**, 147203 (2016).
- [100] X. Zhang, Y. Zhou, and M. Ezawa, Antiferromagnetic Skyrmion: Stability, creation and manipulation, *Sci. Rep.* **6**, 24795 (2016).
- [101] C. Jin, C. Song, J. Wang, and Q. Liu, Dynamics of antiferromagnetic Skyrmion driven by the spin Hall effect, *Appl. Phys. Lett.* **109**, 182404 (2016).
- [102] M. Baćani, M. A. Marioni, J. Schwenk, and H. J. Hug, How to measure the local Dzyaloshinskii-Moriya interaction in Skyrmion thin film multilayers, [arXiv:1609.01615](https://arxiv.org/abs/1609.01615).
- [103] A. L. Hodgkin and A. F. Huxley, A quantitative description of membrane current and its application to conduction and excitation in nerve, *J. Physiol.* **117**, 500 (1952).
- [104] C. Koch and I. Segev, *Methods in Neuronal Modeling: From Ions to Networks* (MIT Press, Cambridge, England, 1998).
- [105] S. Li, W. Kang, Y. Huang, X. Zhang, Y. Zhou, and W. Zhao, Magnetic Skyrmion-based artificial neuron device, *Nanotechnology* **28**, 31LT01 (2017).
- [106] U. Röblier, A. Bogdanov, and C. Pfleiderer, Spontaneous Skyrmion ground states in magnetic metals, *Nature (London)* **442**, 797 (2006).
- [107] W. Koshibae and N. Nagaosa, Creation of Skyrmions and anti-Skyrmions by local heating, *Nat. Commun.* **5**, 5148 (2014).
- [108] J. Hagemester, N. Romming, K. von Bergmann, E. Vedmedenko, and R. Wiesendanger, Stability of single Skyrmionic bits, *Nat. Commun.* **6**, 8455 (2015).
- [109] A. Siemens, Y. Zhang, J. Hagemester, E. Vedmedenko, and R. Wiesendanger, Minimal radius of magnetic Skyrmions: Statics and dynamics, *New J. Phys.* **18**, 045021 (2016).
- [110] H. Oike, A. Kikkawa, N. Kanazawa, Y. Taguchi, M. Kawasaki, Y. Tokura, and F. Kagawa, Interplay between topological and thermodynamic stability in a metastable magnetic Skyrmion lattice, *Nat. Phys.* **12**, 62 (2016).
- [111] G. Yin, Y. Li, L. Kong, R. K. Lake, C.-L. Chien, and J. Zang, Topological charge analysis of ultrafast single Skyrmion creation, *Phys. Rev. B* **93**, 174403 (2016).
- [112] A. Vansteenkiste, J. Leliaert, M. Dvornik, M. Helsen, F. Garcia-Sanchez, and B. Van Waeyenberge, The design and verification of MuMax3, *AIP Adv.* **4**, 107133 (2014).
- [113] D. E. King, DLIB-ML: A machine learning toolkit, *J. Mach. Learn. Res.* **10**, 1755 (2009).
- [114] COMSOL Inc., *COMSOL MULTIPHYSICS User's Guide* (Version 4.3a) (COMSOL, Inc., Burlington, MA, 2012), p. 39.
- [115] A. Bogdanov and A. Hubert, Thermodynamically stable magnetic vortex states in magnetic crystals, *J. Magn. Magn. Mater.* **138**, 255 (1994).
- [116] A. Thiaville, S. Rohart, É. Jué, V. Cros, and A. Fert, Dynamics of Dzyaloshinskii domain walls in ultrathin magnetic films, *Europhys. Lett.* **100**, 57002 (2012).
- [117] G. Gioia and R. D. James, Micromagnetics of very thin films, *Proc. R. Soc. A* **453**, 213 (1997).
- [118] H. Knüpfel, C. B. Muratov, and F. Nolte, Magnetic domains in thin ferromagnetic films with strong perpendicular anisotropy, [arXiv:1702.01980](https://arxiv.org/abs/1702.01980).
- [119] C. B. Muratov and V. V. Slastikov, Domain structure of ultrathin ferromagnetic elements in the presence of Dzyaloshinskii-Moriya interaction, *Proc. R. Soc. A* **473**, 20160666 (2017).